THE ASTROPHYSICAL JOURNAL, 541:468–488, 2000 September 20

EXCITATION OF CHROMOSPHERIC WAVE TRANSIENTS BY COLLAPSING GRANULES

R. SKARTLIEN[1]
Institute of Theoretical Astrophysics, P.O. Box 1029, Blindern, N-0315 Oslo, Norway
R. F. STEIN
Department of Physics and Astronomy, Michigan State University, East Lansing MI 48804
AND
Å. NORDLUND
Theoretical Astrophysics Center and Astronomical Observatory, Juliane Maries Vej 30, DK-2100 Copenhagen Ø, Denmark
Received 2000 January 18; accepted 2000 April 14

ABSTRACT

The excitation of acoustic waves is studied using three-dimensional numerical simulations of the nonmagnetic solar atmosphere and the upper convection zone. Transient acoustic waves in the atmosphere are excited at the top of the convective zone (the cooling layer) and immediately above in the convective overshoot zone, by small granules that undergo a rapid collapse, in the sense that upflow reverses to downflow, on a timescale shorter than the atmospheric acoustic cutoff period (3 minutes). These collapsing granules tend to be located above downflows at the boundaries of mesogranules where the upward enthalpy flux is smaller than average. An extended downdraft between larger cells is formed at the site of the collapse. The waves produced are long wavelength, gravity modified acoustic waves with periods close to the 3 minute cutoff period of the solar atmosphere. The oscillation is initially horizontally localized with a size of about 1 Mm. The wave amplitude decays in time as energy is transported horizontally and vertically away from the site of the event. Observed "acoustic events" and darkening of intergranular lanes could be explained by this purely hydrodynamical process. Furthermore, the observed "internetwork bright grains" in the Ca II H and K line cores and associated shock waves in the chromosphere may also be linked to such wave transients.

Subject headings: convection — hydrodynamics — Sun: atmosphere — Sun: granulation — Sun: oscillations — waves

1. INTRODUCTION

This work aims at a better understanding of the generation of *nonmagnetic* acoustic waves in the solar convection zone and their implications for the overlying photosphere and chromosphere. It is well known from the theory of acoustics that turbulent Reynolds stresses (e.g., a jet-stream) and nonadiabatic processes (e.g., a heat source) produce waves (Lighthill 1952). Generation of acoustic waves by turbulence in the solar convection zone has been studied by, e.g., Stein (1967), Goldreich & Kumar (1990), and Musielak et al. (1994). The approach has been to combine a prescribed turbulence spectrum (e.g., a Kolmogorov spectrum) with Lighthill's theory of sound generation to make a statistical prediction of the wave flux. Sound generation in the convection zone via localized surface cooling, has been modeled by Rast (1999). This work explains the mechanisms that generate acoustic waves when a cool, downgoing thermal plume is initiated. Recently, Nordlund & Stein (2000) and Stein & Nordlund (2000) have used numerical simulations of solar convection to calculate the energy input to acoustic waves by stochastic, nonadiabatic pressure (entropy) fluctuations produced by the interaction of the convective motions and radiation near the solar surface.

If the wave generation is essentially random both in space and time (as is expected when the sources consist of small-scale turbulence), then the resulting waves in the photosphere and chromosphere will have a random distribution, with no obvious isolated sources. The "acoustic events" observed by Rimmele et al. (1995) and Espagnet et al. (1996) show, in contrast, spatially localized wave transients that stand out clearly from the random background field. The observed localized brightenings in the cores of the chromospheric Ca II H and K lines (see Rutten & Uitenbroek 1991) strengthens this view. They imply vertically propagating, spatially localized chromospheric shock-waves that originate from lower amplitude waves in the photosphere or upper convection zone (Carlsson & Stein 1997). These large-scale "acoustic events" therefore suggest larger scale convective processes such as thermal plumes or rapid changes in the granulation. We have sought such "acoustic events" in simulations of the upper solar convection zone and overlying atmosphere up to midchromospheric heights (1.5 Mm above continuum optical depth unity), with the aim of detecting the convective wave sources.

The granular pattern observed on the solar surface is the visible manifestation of the underlying convection. It is a result of mass conservation and the balance between upward transportation of internal energy and radiative cooling. An imbalance here results in a change of granular morphology, and an accompanying adjustment of pressure to restore a stable configuration. Excitation of pressure waves is thus expected. Granule evolution has a typical pattern. As a granule expands, the upflow velocity in the central parts is reduced (see Nordlund 1985; Rast 1995; Stein & Nordlund 1998). The reduced upward internal energy flux no longer balances the surface radiative cooling, and the temperature decreases. The low-temperature, cooled gas has reduced opacity (mainly due to H^- opacity that is proportional to $\sim T^8$) and becomes transparent, so that the underlying gas also cools radiatively. The cooling

[1] Present address: Joint Institute for Laboratory Astrophysics, Campus Box 440, University of Colorado, Boulder, CO 80309-0440; roarsk@hao.ucar.edu.

stops when the gas temperature reaches the radiation equilibrium temperature of the atmosphere above the granule. Downgoing, thermal plumes can be initiated locally in the expanding granule by this cooling process.

As the gas cools, its density increases and gravity brakes the upflow further. This "cooling erosion" of a granule splits it into several smaller fragments (e.g., Nordlund 1985). Some of these fragments have high enough upward energy flux to expand until they also undergo a new splitting process. The smaller fragments diminish in size until they finally vanish or collapse, and leave behind a stronger intergranular downflow.

The "acoustic events" of Rimmele et al. (1995), are typically found near intergranular downflows. These events could therefore be consistent with the picture of small granule fragments that collapse while generating waves. When the timescale of the changes to these small granule fragments is shorter than the atmospheric cutoff period, propagating pressure waves are launched that eventually shock at chromospheric heights.

The organization of the paper is as follows. The simulation is briefly described in § 2. The properties of "acoustic events" are presented in § 3. The collapse of small granules is discussed in § 4. The excitation of atmospheric waves is described in § 5. The results are summarized in § 6.

2. NUMERICAL SIMULATION

The three-dimensional solar convection model of Nordlund & Stein (1990) has been extended in the vertical direction, to include the chromosphere up to a height of 1500 km above the "cooling layer" at $\tau = 1$. Equations of mass, momentum, and energy are solved (see Nordlund & Stein 1990 for details). Ionization and excitation of hydrogen and other abundant atoms, and formation of H_2 molecules, is included in the equation of state (Gustafsson 1973). The original version of the code assumed nongray, LTE radiation without scattering. The inclusion of the dilute upper atmosphere requires a treatment of photon scattering because a non-negligible fraction of the photons are scattered rather than being absorbed by the gas, and these scattered photons do not contribute to energy exchange with the gas.

This three-dimensional radiation-scattering problem is solved using a statistical approach, so as to minimize computer time (Skartlien 2000). First, wavelength dependent LTE opacities are sorted into four group mean opacities according to their magnitudes as in Nordlund (1982). The wavelength dependent opacities come from the opacity distribution functions of Gustafsson et al. (1975), which include relevant opacities for solar conditions. The same wavelength binning is applied to a new set of quantities: group mean thermal emission, and mean photon destruction probabilities. All opacity dependent quantities are precalculated and stored in a lookup table, that also includes the equation of state. At each time step, there is one radiation problem for each opacity group corresponding to a "two-level" source function with coherent scattering. The radiation flux divergence at each time step is found after iterating in each group. The iterations are accelerated by a new method designed for this specific problem (Skartlien 2000).

The lower boundary is located 1500 km below the top of the convection zone. This gives a total vertical extent of 3 Mm, covering 2 orders of magnitude in density in the convection zone, and 5 orders of magnitude in the atmosphere. The horizontal extent is 6×6 Mm, which covers typically five large granular cells.

The lower boundary is reflective for sound waves, such that a resonant cavity is formed with the photosphere as the upper reflective boundary for long period waves that are evanescent in the photosphere. The depth of the model convection zone is chosen such that the period of the lowest frequency radial (vertical) mode is 5 minutes, so as to mimic 5 minute solar p-modes, and their influence on atmospheric dynamics. Two low-resolution runs were calculated, with $32 \times 32 \times 100$ grid points. One run has the lowest possible viscosity without generating ripples, and one has higher viscosity to damp out long lived wave interference. These have a duration of 62 and 101 minutes of solar time, respectively. One higher resolution, low-viscosity run with $64 \times 64 \times 100$ grid points was calculated as a validity check on the low-resolution runs.

The processing time is large due to the radiation iterations. The hydrodynamic calculations take a negligible time in comparison. The high-resolution run used 10,000 CPU hours for 1 hour of solar time, on a SGI CRAY ORIGIN 2000 parallel computer. The radiation part of the code is run in parallel, with simultaneous computations for the radiation along different rays through the domain. The CPU time scales approximately linearly with the number of spatial grid points and angle points (rays) used for the radiation.

3. ACOUSTIC EVENTS

Acoustic events are identified observationally by Restaino, Stebbins, & Goode (1993) and Rimmele et al. (1995), as peaks in their definition of the vertical acoustic flux,

$$F_{\rm ac} = \rho V_z^2 c_{\rm grp} = -\frac{\gamma P V_z^2}{\omega}\frac{\partial \phi}{\partial z} \quad .$$

Here V_z is the Doppler velocity amplitude (at a given depth in a line), $\partial\phi/\partial z$ is the observed vertical velocity phase gradient (from two different depths in the line), ρ is the average density and P is the average pressure at the height of formation of the observed depth in the line, γ is the ratio of specific heats, and ω is the wave frequency (taken as the frequency of the p-mode power maximum ≈ 0.02 s^{-1}) (Rimmele et al. 1995).

Acoustic events are identified in the simulations as upward followed by downward pulses in the vertical velocity, u_z, the vertical kinetic energy flux, $\rho u^2 u_z$, or the vertical acoustic flux,[2] $P u_z$ at a height of 0.7 Mm above the visible surface (Fig. 1). By this height the traveling waves have steepened and the p-mode and convective overshoot velocities have decreased to the point where waves dominate.

Acoustic events, both observed and simulated, are correlated with a darkening in the continuum intensity and with

[2] We note that the interpretation of $P\boldsymbol{u}$ (or its vertical component Pu_z) as wave energy flux is only meaningful in the absence of convective flow fields, or when the convective flow field evolves on a much longer timescale in comparison to the period of the waves considered. This fact is often overlooked when acoustic fluxes with oscillating components of, e.g., 5 minutes or 3 minutes are measured from observations. These periods are clearly not much shorter than the typical lifetime of granular cells. The oscillating velocity pattern seen at $z = 0.7$ Mm in the simulations can be attributed mainly to wave motion since the velocity from the convective overshoot is dramatically reduced above $z = 0.5$ Mm, and it is relatively small in comparison to the oscillation amplitudes caused by the events.

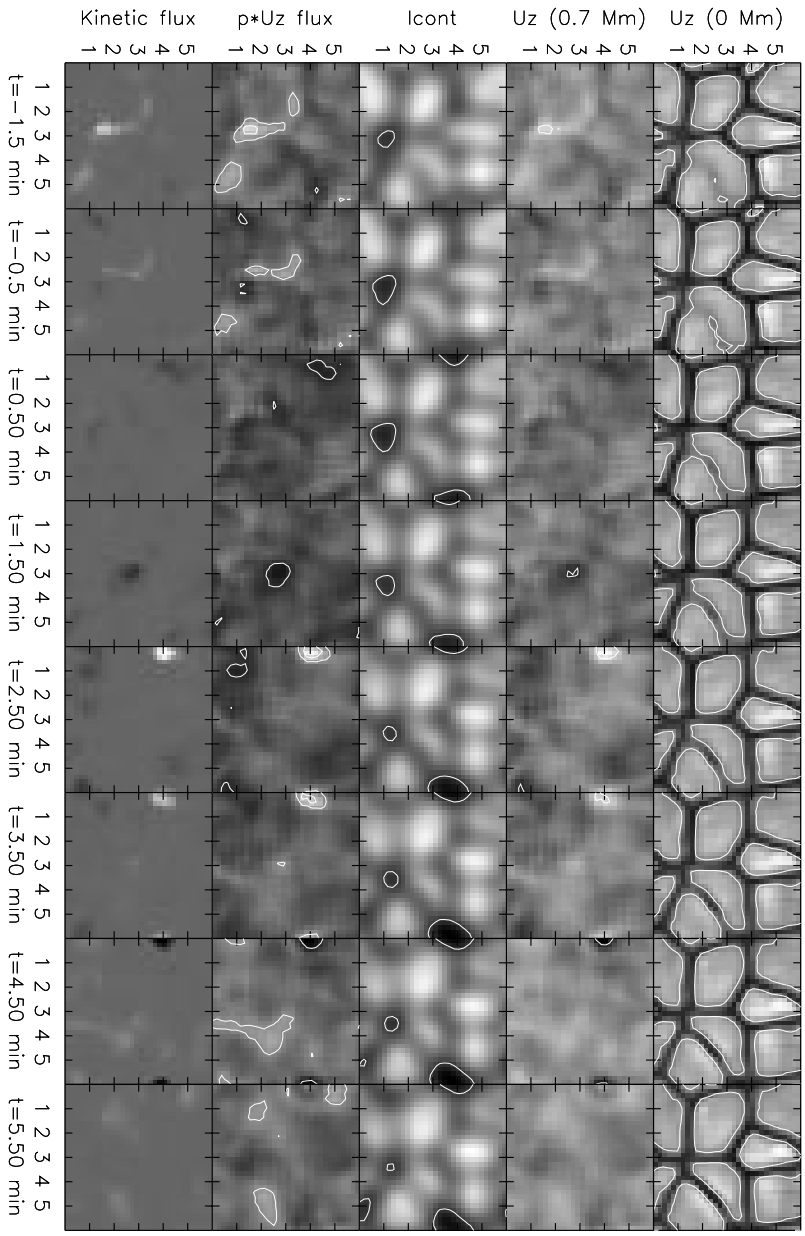

FIG. 1.—Observers view. Each column shows the evolution of different quantities in an acoustic event. Each image is a horizontal slice that covers the full horizontal extent of 6 × 6 Mm, with x-direction running horizontally and the y-direction running vertically. The time series starts at the top and continues downward. The quantities are, starting at the rightmost column: [U_z(0 Mm)] Vertical velocity in the cooling layer at $z = 0.0$ Mm. The contour shows zero velocity. Upward velocity corresponds to lighter shades of gray. A small granule disappears at $t = 0.0$ minutes, at the coordinate (4.0,0.5) Mm (*at the border between the images in the upper right corner*). [U_z(0.7 Mm)] Vertical velocity at 0.7 Mm above the cooling layer. The contours show ± 0.6 times the maximum velocity in the series. After the granule disappears, we see an upward velocity pulse at $t = 2.5$ minutes, also at the position (4.0, 0.5) Mm. A downward pulse follows, which is seen at $t = 4.5$ minutes. A circular wave pattern can be seen at $t = 5.5$ minutes. (Icont) Smeared continuum/granulation intensity. The contour marks 0.9 times the average intensity. An apparent dark spot grows after the granule has disappeared. [Pu_z-flux: (0.7 Mm)] The contours show the levels ± 0.6 and ± 0.3 times the maximum flux in the series. The upward flux is larger than the downward flux. (Kinetic flux) Vertical kinetic energy flux $(\frac{1}{2}\rho u^2)u_z$ at 0.7 Mm. A splitting granule is also seen in the figure, but it does not produce a highly localized, high-energy flux density, pulse. Low-energy fluctuations superposed on the images that are not directly related to the vanishing granule events also occur.

downflowing fluid at the visible surface. In the simulations, they are related to rapid changes in the granular pattern—the disappearance of small granules or the fragmentation of larger granules. The strongest, most localized, events correspond to the rapid vanishing of small, isolated, granules. Small fragments of larger granules that disappear in intergranular lanes immediately after a splitting process are sometimes also associated with an event, but these are larger and weaker. Horizontal wave components are detectable in some of these events, and appear as horizontally expanding rings or ellipses (with stronger amplitudes on one side of the event than the other).

The time sequence of a typical acoustic event initiated by the vanishing of a small granule is as follows: a small granule in the vertex of intergranular lanes shrinks horizontally and disappears with upflow reversing to downflow on a timescale short compared to the acoustic cutoff period [Fig. 1, $t = 0.0$ minutes, coordinates (4.0,0.5) Mm at the border between the images in the upper right corner]. A dark spot in the smeared continuum intensity starts to

develop around this vertex after the granule has disappeared. The overlying atmosphere, at $z = 0.7$ Mm above the vertex, responds with a relatively small downward velocity as seen in the figure at $t = 0.5$ minutes. A larger upward velocity pulse follows at $t = 2.5$ minutes. A succeeding smaller downward velocity is found at $t = 4.5$ minutes. Then a decaying oscillation follows at this position. The horizontal size of the oscillating spot is initially about 1.0 Mm, but expands when a circular shaped wave propagates outward in the horizontal direction. This is seen at $t = 5.5$ minutes in the figure. The vertical wave energy flux Pu_z and kinetic energy flux $\rho u^2 u_z/2$ at $z = 0.7$ Mm show upward and downward pulses in phase with the velocity. The initial upward flux has larger magnitude than the following downward pulse, so that energy is transported upward at this height.

Velocities in the granules at $z = 0.0$ Mm and the atmosphere above (at $z = 0.7$ Mm) are shown in Figure 2 for 6 different events found during 65 minutes of solar time in the simulation. These velocities are for horizontal positions defined by the centers of the vanishing granules at $z = 0.0$ Mm. The time delay of the maximum upward velocity pulse at $z = 0.7$ Mm ranges from 1 to 3 minutes after granular velocity reversal at $t = 0.0$ minutes. There is a weak tendency for larger maximum upward velocity pulses to have longer time delays. After the upward pulse, a decaying oscillation starts.

The granular velocity for the events evolves almost linearly in time around $t = 0.0$ minutes, which corresponds to ballistic (parabolic) motion. Most of the velocity jump is covered within a time span of 2 minutes. The steep decline of the granular velocities is evidently connected to the wave transient at $z = 0.7$ Mm, as seen in the figure. We also note that the upflow velocity in the granule is *increasing* before the collapse. The different strengths of the events (as measured by the velocity magnitude at $z = 0.7$ Mm) are not obviously linked to the timescale or magnitude of the granular velocity jump.

The average response of the vertical velocity at $z = 0.7$ Mm, is also shown in Figure 2. Here the velocity sequences are aligned such that maximum upward velocities coincide before averaging, since we have different time delays for the maximum. On the average, the atmosphere responds to the newly formed downdrafts with a delayed upward velocity pulse that is larger than the initial downward velocity. On the average, the first upward velocity phase lasts for 2 minutes, with a maximum amplitude of 1.25 km s^{-1}. There is a preceding downward velocity of -0.5 km s^{-1} and a larger succeeding downward velocity of -0.75 km s^{-1}.

Atmospheric oscillations may exist prior to the excitation of the events. In these cases, the interference from atmospheric oscillations modulates the velocity signal at $z = 0.7$ Mm, which makes it difficult to determine a correlation of wave velocities at 0.7 Mm with granule velocity reversal. The amplitude of the atmospheric velocity pulse is in these cases dependent on whether the excitation comes in phase or out of phase with the preceding atmospheric oscillation. Despite the modulation by interference, the average velocity curves in the lower right panel in Figure 2, should give a reliable picture of the atmospheric velocity response.

Energy is fed into the 3 minute rather than the 5 minute oscillation. This can be seen by bandpass-filtering the vertical velocity at $z = 0.7$ Mm into two frequency bands centered at 5 and 3 minutes. The widths of the filters are chosen such that they cover most of the power in the neighborhood of these periods in the Fourier domain. We then compute the time dependent envelope for each of the two bandpass filtered velocity signals.[3] We apply this procedure to the two large events (A) and (B) (Fig. 3). The envelope of the 3 minute band grows from $t = 0.0$ minutes (when the cell collapses) and reaches the peak at $t = 5.0$ minutes, after

[3] The envelope $V(t)$ is just the modulus of the complex, analytical signal $u(t) - i\boldsymbol{H}[u(t)]$. The real part u is the bandpass filtered velocity, and the imaginary part being minus the Hilbert transform of u.

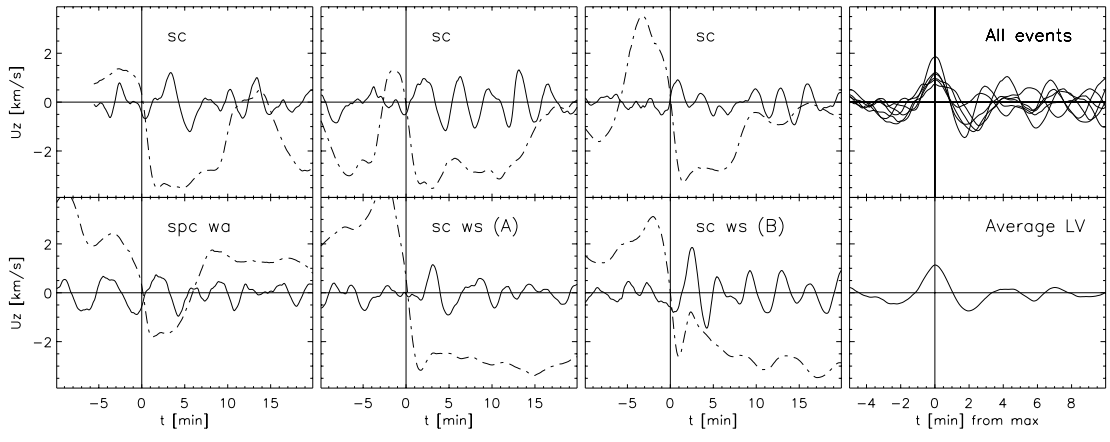

FIG. 2.—Six events in the low-viscosity run (65 minutes solar time). The solid line is the vertical velocity at $z = 0.7$ Mm, and the dash-dotted line the vertical velocity in the granule at $z = 0.0$ Mm. Each velocity signal is measured at the horizontal position centered above the vanishing granule. At $t = 0.0$ minutes, the vertical velocity in the granule reverses from upward (positive) to downward (negative) velocity. The two rightmost panels show all velocity curves for the vertical velocity at $z = 0.7$ Mm, and the corresponding average. The time axis is in this case centered on maximum upward velocity for each individual event. The codes in each panel for the individual events are as follows: (sc) single granule that vanishes; (spc) splitting granule, which means that a fragment separates from a larger granule and vanishes in a downdraft immediately afterward; (ws) circular shaped, horizontally propagating wavefront at $z = 0.7$ Mm; (wa) asymmetric wavefronts, larger on one side of the event. The time delays for the upward velocity pulse in the atmosphere for the events, lie in the interval [1, 3] minutes, with pulse magnitudes in the interval [1, 2] km s^{-1}. On the average (*lower right panel for all events*), the upward pulse lasts for about 2 minutes, with an amplitude of 1.25 km s^{-1}. We see a preceding downward velocity of -0.5 km s^{-1} and a larger succeeding downward velocity of -0.75 km s^{-1}. The granular velocity evolves almost linearly in time around $t = 0.0$ minutes when the timescale is shortest. Most of the velocity jump is covered within a timespan of 2 minutes.

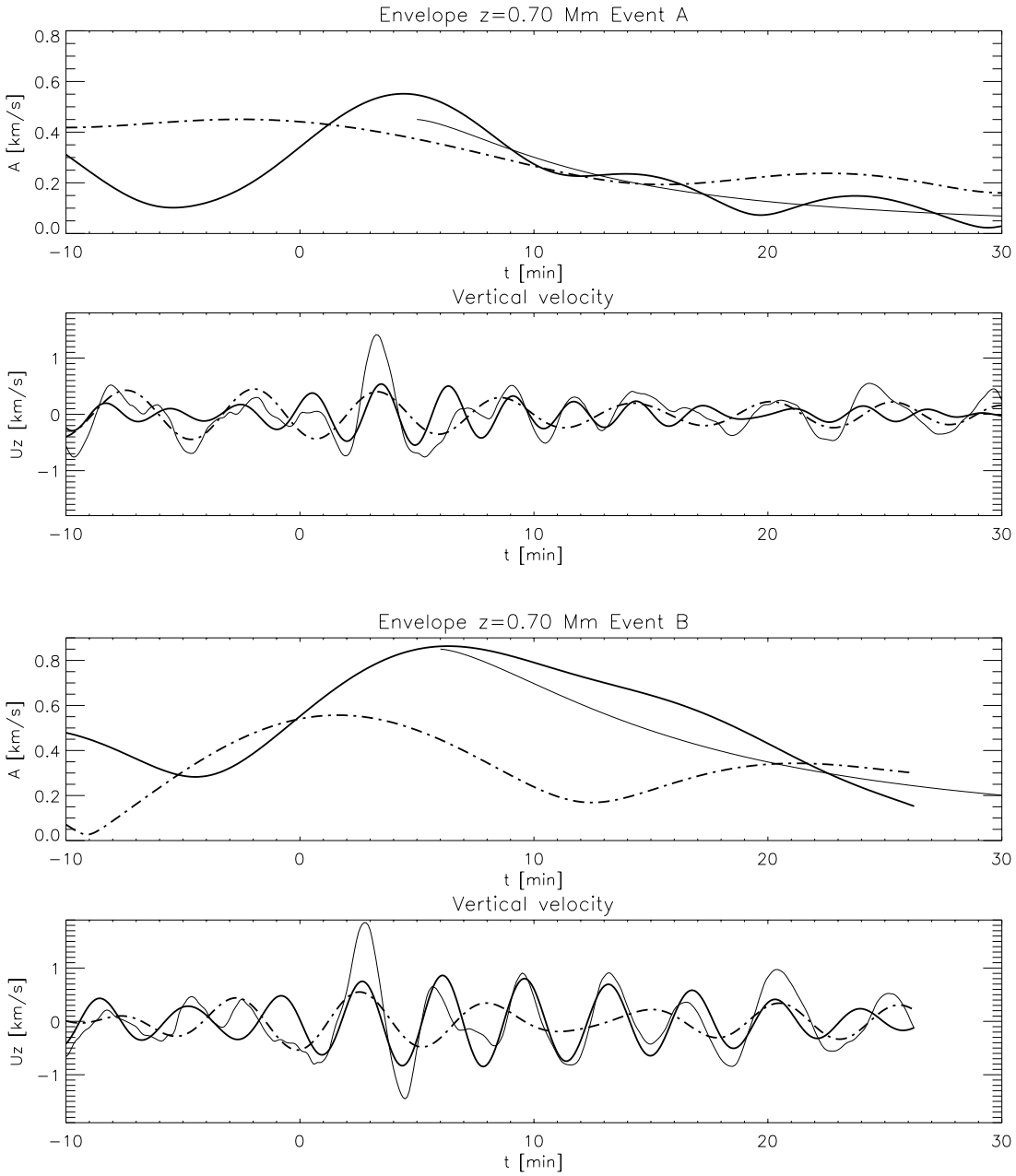

FIG. 3.—Envelope decomposition of events A and B. The upper panel for each event shows the envelope of the vertical velocity oscillation in the 5 minutes (*dash-dotted line*) and 3 minutes (*solid line*) frequency bands. The velocity signal is taken at $z = 0.7$ Mm, above the vanishing granule. The time is zero when the granule vanishes at $z = 0.0$ Mm. The thin solid line indicates the best fit to a $t^{-3/2}$ decay of the envelope. This is the analytical solution of the asymptotic decay of the 3 minute eigenperiod, as described by the Klein-Gordon equation, when this is driven by sinusoidal forcing starting at $t = 0.0$ minutes. It is noted that the amplitude of the envelope for the 3 minute band increases at the onset of the events, reaches a maximum at about $t = 5.0$ minutes and then decays approximately as predicted from linear theory. The envelope for the 5 minute band is damped rather than amplified after the onset of the acoustic events. Hence, the events are mainly exciting oscillations in the 3 minute band. The lower panel for each event shows the bandpass filtered velocities that correspond to the envelopes in the upper panel. The envelopes are enclosing these "wave packets." The original velocity signal is shown in addition, by the thin solid line. It is also noted that the maximum velocity amplitude (at about $t = 3.0$ minutes) precedes the peak in the envelope in the 3 minute band.

which it decays. In contrast, the envelope of the 5 minute band decays immediately after $t = 0.0$ minutes. The 5 minute envelope magnitudes are also insensitive to the velocity amplitude of the events at $t = 0.0$ minutes (*thin line in the lower panels*), as opposed to the 3 minute envelopes.

The asymptotic $t^{-3/2}$ decay for the 3 minute eigenoscillation from linear and plane parallel theory (Klein-Gordon equation) (Lamb 1908 and, e.g., Kalkofen et al. 1992) fits well with the 3 minute envelope for event (A) but not very well for event (B). Discrepancies from the smooth, analytical prediction can also here be due to interference from other waves that are not excited by the events. The kinetic energy density in the 3 minute oscillatory wake generated by a localized, impulsive source is in theory concentrated above and below the source (Kato 1966). This vertical focusing is also suggested by the relatively small horizontal size (about 1 Mm) of the region of upward wave energy flux in the events (Fig. 1).

4. GRANULE COLLAPSE

Acoustic events are initiated primarily by the collapse of small granules, where the vertical velocity at the surface rapidly reverses from upflow to downflow. The main goal of this paper is to understand how and why waves in the convectively stable atmospheric layers are excited when small granules disappear. We start by analyzing the process of granule collapse.

4.1. *Granule Evolution Is Controlled by Mesogranule Flow*

Granules evolve typically as follows: expanding granules split, and form smaller granules. These contract and vanish, or expand and split, depending on their location. (See Hirzberger et al. 1999 for a statistical treatment of observed solar granulation.) The simulations show that expanding granules are located, in a statistical sense, above subsurface upflows, while collapsing (contracting) granules are located above subsurface downflows. The upward enthalpy flux density is higher beneath expanding granules, and lower or even negative below collapsing granules. This correlation is measured as deep as 1 Mm below the surface. This suggests that granule evolution is also controlled by subsurface flow, not only surface dynamics and radiative cooling.

Granule evolution can be studied in several ways. To obtain some statistical results from the data, we selected 16 granules (10 collapsing and 6 expanding) from the $64 \times 64 \times 100$ simulation. We found that granules respond strongly to the subsurface flow.

1. Collapsing granules are, on the average, located above subsurface downflows, and some tend to get advected toward the site of collapse (Figs. 5 and 6). Expanding granules are located above subsurface upflows. Figure 4 also shows that collapsing granules are located approximately above these downdrafts at $z = -1.0$ Mm and near intergranular vertices at $z = -0.5$ Mm. As seen by the arrow directions, there is also a tendency of horizontal advection of the granules toward these locations.

2. The upward enthalpy flux is, on the average, smaller beneath collapsing granules than beneath expanding granules. The average time evolution of collapsing and expanding granules is shown in Figure 7.

The enthalpy flux $F_h = (\rho e + P)u_z$ in subsurface layers is measured in the horizontal area corresponding to the projection of the surface granular area, thus measuring flux immediately below the upflow. The average enthalpy flux density $\langle F_h \rangle$ follows from horizontal averaging in these areas and is denoted by "the enthalpy flux" in the following. Positive values mean upward flux.

For collapsing granules: The flux at 0.5 Mm below the surface is positive and decreases with time, while at 1.0 Mm it is typically negative. For expanding granules: The flux is positive and roughly constant at both depths. Figure 8 shows the correlation between surface area and subsurface enthalpy flux for all times.

In addition to the subsurface effect of reduced upward energy flux, we also note the effect of merging downflows, which is probably important in the final stages of granule collapse. Rast (1998) has shown that two-dimensional downflows merge if the only effect is the mutual advection in their respective flow fields. Ploner et al. (1998) address granule evolution with a two-dimensional radiation hydrodynamic model and also find that merging downflows is a typical process. It is therefore reasonable to believe that a small granule tends to collapse also by the effect of attracting downflows, if not counteracted by excessive upward enthalpy flux between the downflows (within the granule).

These two effects can be expressed by a phenomenological equation, of the form

$$\frac{dA}{dt} = -\frac{\alpha}{A} + \beta(F_h - \overline{F_h}) , \tag{1}$$

where the granule surface area A evolves in time by (1) perturbations in upward enthalpy flux F_h, relative to the horizontal average $\overline{F_h}$ (if the enthalpy flux into one granule is lower than $\overline{F_h}$, then the granule would collapse), and by (2) mutual advection of close downflows represented by α/A (the downflows attract more effectively the closer they are).

The constant α depends upon how "effective" the horizontal advection of the downflows is, since in the small granule regime where advection dominates, $V_{\text{advection}} = dr/dt \sim \alpha/r^3$ (with $A \sim r^2$). The constant β represents the fraction of the energy flux deposited in the granular volume (ingoing fluxes at the bottom F_h minus outgoing fluxes horizontally and at the surface as radiative cooling).

This model clearly gives room for many different evolution patterns, depending on the upward energy flux where the granule is located, relative to the merging effect. One important point is that expansion and contraction are controlled by the same processes and are not due to different phenomena. There is not even a characteristic area (size) that can be used to separate potentially expanding from potentially collapsing granules. This is illustrated by considering the "equilibrium area," that brings the source and sink terms in the evolution equation in balance, such that $dA/dt = 0$. The flux F_h(eq.) and area A(eq.) in "equilibrium," is

$$F_h(\text{eq.}) = \frac{\alpha}{\beta A(\text{eq.})} + \overline{F_h} . \tag{2}$$

This equilibrium is, however, unstable; if the flux is lowered, then the advection term dominates and the area decreases.

The equilibrium condition separates the collapsing and expanding domains surprisingly well. Figure 8 shows the flux F_h(eq.) as function of A(eq.), with the fitting constants $\alpha = 0.135$, $\beta = 0.027$, together with the data. The high flux values in the upper left corner is now explained since it takes a relatively large flux to balance the attracting downflows surrounding a small granule. We note that the fit is not as good for larger granule sizes, as merging downflows/collapse of nearby granules might enhance the expansion, such that the upward flux need not be as large (hence, one should consider the evolution equation to describe "local" merging effects only).

It is interesting to note that the flux term in the evolution equation can be viewed as a contribution with "memory," since the upward flux is dependent on subsurface downflows which were created in the past by surface downflow/plume formation. The advection/merging term may be interpreted as a "memoryless" surface contribution. There is, however, horizontal coupling at the surface since the collapse of neighbor granules may lead to expansion.

Taking these results into consideration, we conclude that granules collapse partly because (1) they are starved for energy and hence lose buoyancy because they lie above or

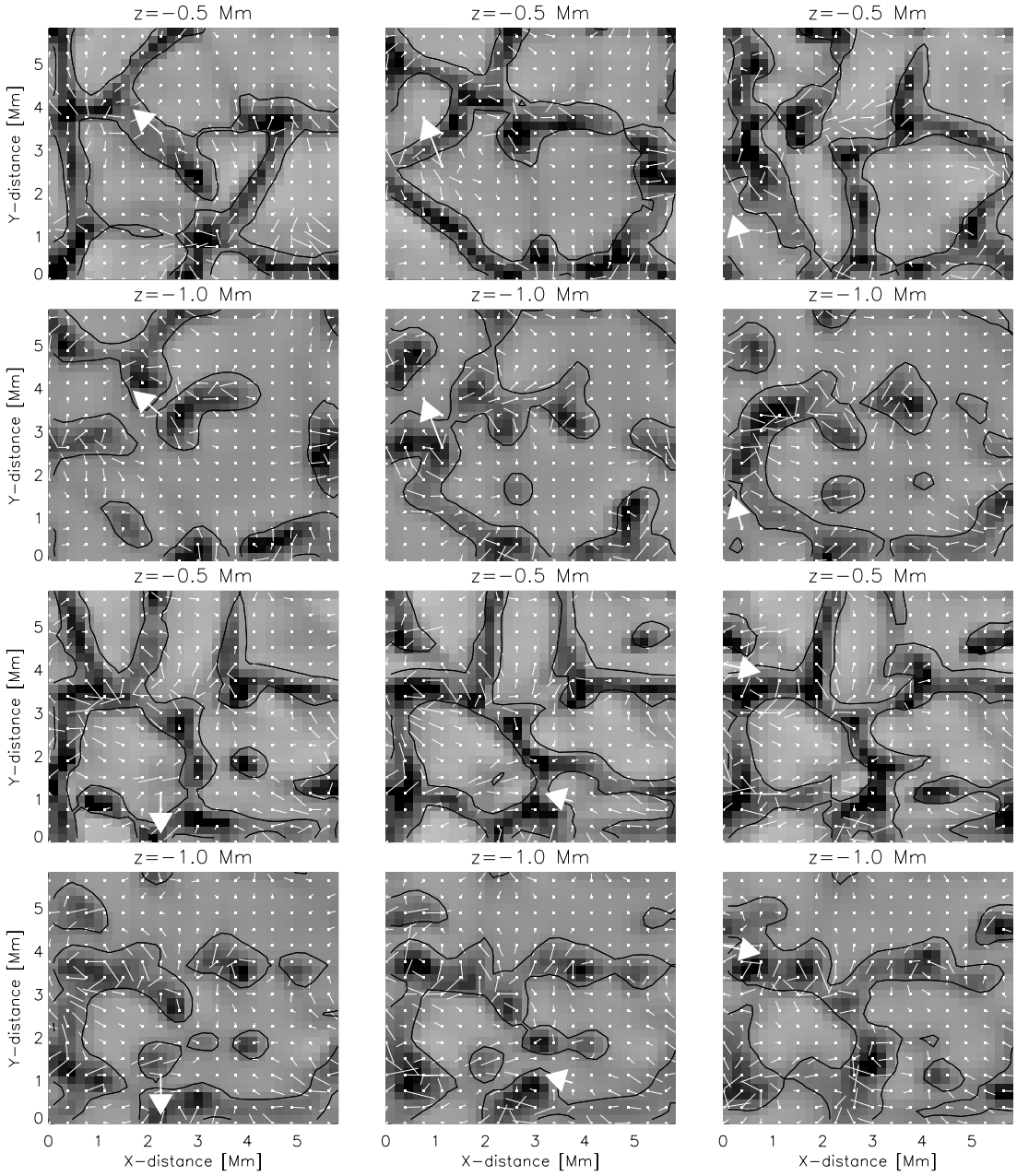

FIG. 4.—Correlation to subsurface flow. *Shaded images*: vertical velocity at 0.5 Mm (*upper images*) and 1.0 Mm (*lower images*) below the surface, with upflow as lighter shades. Corresponding images (two simultaneous images for each event) are vertically aligned. *Black contours*: zero vertical velocity. Velocity vectors for horizontal velocities are white "flags" pointing in the "downwind" direction. White arrows show the motion of the central parts of small granular cells at the surface (0.0 Mm), from where the cell splits from a larger cell (starting point), to the point where they collapse (end points). The time and position of collapse is defined by the last measurement of upward velocity at the surface. All velocity images are taken at the time of cell collapse at the surface. The horizontal position at the surface where granules collapse tends to be located above, or near subsurface downflow. In most cases, there is also a tendency of "attraction" to these locations, as seen by the arrows.

near a mesogranule boundary downflow, and (2) they are squeezed by expansion of surrounding granules (with greater energy flow) and the tendency for downflows surrounding a small granule to merge.

4.2. *Pressure and Buoyancy Forces*

We now turn to the details of granule collapse. Since flows are driven by pressure gradients and buoyancy forces, we study the sources of pressure, pressure gradient and density changes. We first give the relevant equations that will be needed in the subsequent discussion.

4.2.1. *Equations*

The vertical component of the equation of motion is

$$\rho \frac{Du_z}{Dt} = -\frac{\partial P}{\partial z} - \rho g + \eta_z = F_z \,, \tag{3}$$

where ρ is the density, D/Dt is the Lagrangian time derivative, u_z is the vertical velocity, P is the pressure, and g is the acceleration of gravity, which is taken as constant in our domain. F_z is the net vertical force per volume unit, and η_z is the viscous force.

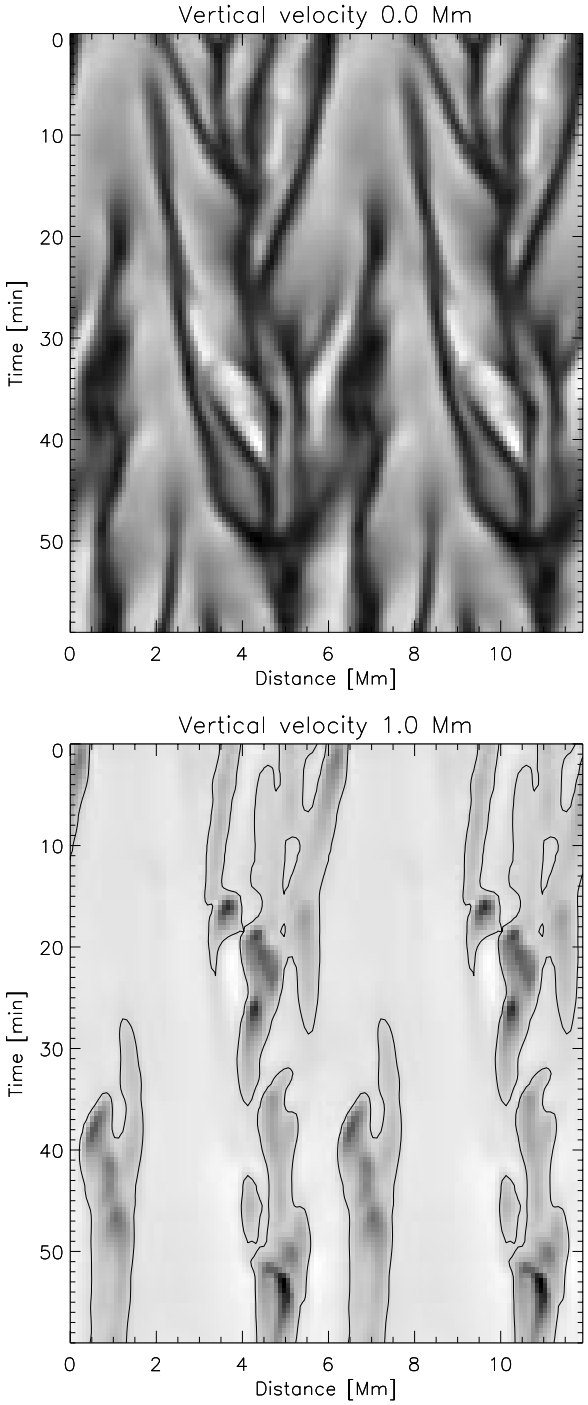

FIG. 5.—Merging downflows. The upper image is the time evolution of the vertical velocity at the surface, as measured along a horizontal line. Downflows are dark and upflows have lighter shades. Collapsing granules correspond to where downflows merge. The merging downflow positions (where granules collapse) are located above subsurface downflows 1.0 Mm below the surface. This is seen in the lower panel, where subsurface downflows are dark regions delineated by a black contour for zero vertical velocity.

Pressure varies due to adiabatic changes (density fluctuations) and nonadiabatic changes (entropy fluctuations). This is given by the first law of thermodynamics in the form

$$dP = c^2 d\rho + (\Gamma_3 - 1)\rho T ds \,, \tag{4}$$

where $c^2 = \Gamma_1 P/\rho$ is the squared sound velocity with $\Gamma_1 = (\partial \ln P/\partial \ln \rho)_s$. $\Gamma_3 - 1 = (\partial \ln T/\partial \ln \rho)_s = (\partial P/\partial e)_\rho/\rho$. e is the specific internal energy; T is the temperature.

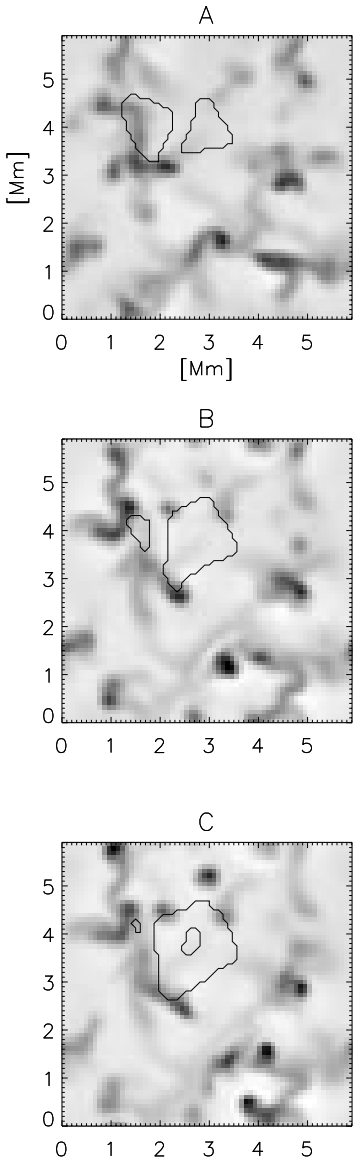

FIG. 6.—Example of granule expansion/collapse. This time series show that the evolution of the granules is not dependent on initial size, but location and upward enthalpy flux. The black contours show two granules (regions with surface upflow), while the image is vertical velocity 1.0 Mm below the surface. Light is upflow and dark is downflow. Image "A" is the initial. Image "B" shows that the granules expand above the upflow and contract above the downflow. Image "C" shows the splitting of the larger granule.

This equation states a relation between thermodynamic variables and therefore holds for the Eulerian time derivatives at any location,

$$\frac{\partial P}{\partial t} = c^2 \frac{\partial \rho}{\partial t} + (\Gamma_3 - 1)\rho T \frac{\partial s}{\partial t} \,. \tag{5}$$

The horizontal and vertical mass flux divergence control the density changes (and therefore also the adiabatic pressure and pressure gradient fluctuations),

$$-\frac{\partial \rho}{\partial t} = \nabla \cdot (\rho \boldsymbol{u}) = \nabla_h \cdot (\rho \boldsymbol{u}_h) + \frac{\partial}{\partial z}(\rho u_z) \,, \tag{6}$$

where ∇_h is the divergence operator acting on the horizontal components $\boldsymbol{u}_h$ of the velocity vector. The time derivative of specific entropy is related to radiative and viscous heat

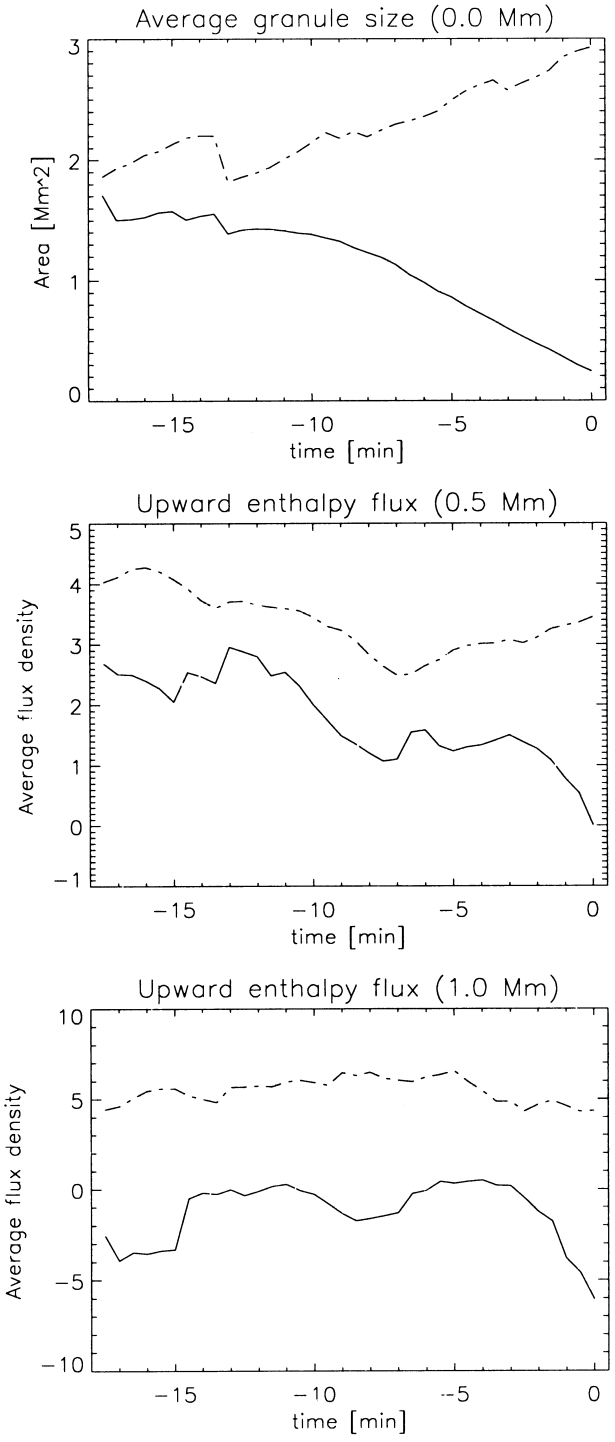

FIG. 7.—Evolution statistics. The upper panel shows the granule size as function of time averaged over all granules. The dashed line is for the expanding, and the solid line for the collapsing granules. The middle and bottom panels show the corresponding enthalpy flux at 0.5 Mm and 1.0 Mm below the surface. The collapsing granules have on the average lower upward flux than the expanding granules. Note that the flux can even be negative below the collapsing granules.

sources and advection of specific entropy by

$$\frac{\partial s}{\partial t} = \frac{1}{T}\,(q_{\rm rad} + q_{\rm visc}) - \boldsymbol{u}\cdot\nabla s\,, \qquad (7)$$

where $q_{\rm rad.}$ and $q_{\rm visc.}$ are radiative and viscous specific heating rates, respectively.

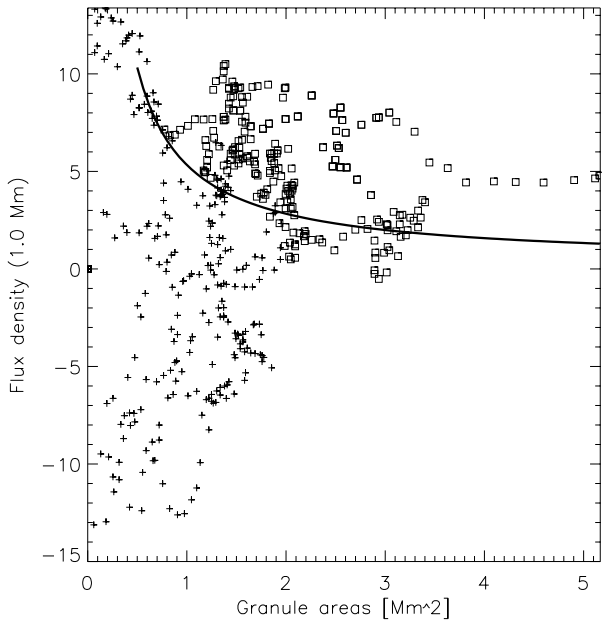

FIG. 8.—Stability model. This scatterplot shows corresponding subsurface flux and surface size for all granules at all times. The squares indicate expanding granules, while the crosses indicate collapsing granules. The thick line is the stability line derived from the phenomenological equation and divides the plot in two regions. Granules above this line should expand, while granules below and to the left of the line should contract. The model fits the data for smaller granule areas and shows that small granules need large upward flux to counteract the effect of merging downflows. The correspondence is poorer at larger granule areas, since granule expansion by neighboring granule collapse is not accounted for in the model. In that case a lower subsurface flux is sufficient to expand the granule.

Using the continuity equation, and the last relation, we can write the time derivative of the pressure as

$$\frac{\partial P}{\partial t} = -c^2\nabla\cdot(\rho\boldsymbol{u}) + (\Gamma_3 - 1)\rho\{q_{\rm rad} + q_{\rm visc} - \boldsymbol{u}\cdot T\nabla s\}\,. \qquad (8)$$

The first term on the right-hand side is the adiabatic contribution from the mass flux divergence (the pressure decreases for a net mass outflow from a volume) and the second term is the nonadiabatic contribution arising from an imbalance between heating/cooling in a volume and the advection of heat into or out of the volume. The adiabatic and nonadiabatic contributions to the pressure are found by integrating equation (5) over time:

$$P_{\rm adiab.}(t) = \int\left\{c_s^2\,\frac{\partial\rho}{\partial t}\right\}dt + \text{const}\,.$$

$$P_{\rm non-adiab.}(t) = \int\left\{(\Gamma_3 - 1)\rho T\,\frac{\partial s}{\partial t}\right\}dt + \text{const}\,. \qquad (9)$$

The rate of change of the vertical pressure gradient is obtained by taking the vertical derivative of equation (5) and can also be split into contributions from adiabatic and nonadiabatic sources,

$$\frac{\partial}{\partial t}\frac{\partial P}{\partial z} = \frac{\partial}{\partial z}\left\{c^2\,\frac{\partial\rho}{\partial t}\right\} + \frac{\partial}{\partial z}\left\{(\Gamma_3 - 1)\rho T\,\frac{\partial s}{\partial t}\right\}. \qquad (10)$$

The adiabatic and nonadiabatic contributions to the pressure gradient are obtained by time integration of equation (10).

4.2.2. *Contributions to Pressure Changes*

The rate of pressure change $\partial P/\partial t$ and the various terms contributing to it are shown in Figure 9 as a function of height and time along a column centered on the acoustic event B. The lower left panel shows $\partial P/\partial t$, and the lower right panel shows the relative pressure perturbation that is its time integral. The contributions to $\partial P/\partial t$ are shown in the top and middle panels. All of these terms have been scaled by an arbitrary factor e^{6z} to normalize the variations over the large height range in the images.

The nonadiabatic contribution,

$$(\Gamma_3 - 1)\rho T \frac{\partial s}{\partial t},$$

(eq. [5]) is shown in the middle left panel. This can be further separated into radiative heating, viscous heating, and advection:

$$T \frac{\partial s}{\partial t} = q_{\text{rad.}} + q_{\text{visc.}} - \boldsymbol{u} \cdot T\nabla s,$$

(eq. [7]). The heat advection term,

$$-\rho(\Gamma_3 - 1)\boldsymbol{u} \cdot T\nabla s,$$

is shown in the upper left panel.[4] The heating term,

$$\rho(\Gamma_3 - 1)(q_{\text{rad.}} + q_{\text{visc.}}),$$

is shown in the upper right panel. A positive contribution from these heating terms can balance expansion work (a negative adiabatic contribution) and/or increase the pressure. The sum of the two terms in the upper panels is equal to the nonadiabatic contribution in the middle left panel. The middle right panel shows the adiabatic contribution:

$$c_s^2 \frac{\partial \rho}{\partial t}.$$

4.3. *The Collapse Process*

Figures 10 and 11 show the fluid acceleration as a function of time in a vertical column centered on the collapsing granule at the instant of collapse ($t = 0.0$) for events (B) and (A). There is an initial upward acceleration below the surface (between $z = -0.1$ Mm to about $z = -0.4$ Mm), from $t = -5.0$ minutes to about $t = -1.0$ minutes. After $t = -1.0$ minutes, upward acceleration reverses to downward. At $t = 0.0$ minutes the upflow in the cooling layer reverses to downflow. The flow patterns in both events (A) and (B) are qualitatively similar, and we choose to discuss event (B) in detail in the following.

The evolution of relative perturbations in pressure, vertical pressure gradient, and buoyancy force, along the vertical column through the collapsing granule, are shown in Figure 12. These perturbations are given by $P/\langle P\rangle - 1$, $(\partial P/\partial z)/\langle \partial P/\partial z\rangle - 1$ and $(g\rho)/\langle \partial P/\partial z\rangle - 1$, respectively, where the brackets denote time averaging. The gravity is normalized with the average pressure gradient, such that the figures can be compared directly in the sense that higher value of the pressure gradient perturbation than the gravity perturbation gives a net upward force. The black contour shows zero perturbations and the white contours, $\pm 5\%$ and $\pm 20\%$ perturbations.

The particle paths for the vertical motion (*white lines*) are diverging in subsurface layers before the collapse, indicating vertical mass flux divergence. Since only small fluctuations in density occur in the convection zone [$\nabla \cdot (\rho \boldsymbol{u}) \sim 0$], the accompanying vertical mass flux divergence is largely compensated by horizontal mass flux convergence of fluid from neighboring granules (Fig. 13).

Now, consider the initial phases, before $t = -2.0$ minutes, and shallow layers, around $z = -0.3$ Mm. A positive pressure perturbation develops around $z = -0.3$ Mm (Fig. 12, *left panel*) that is larger than the pressure perturbation above and below this level. This is mainly due to the increasing density (adiabatic change) at this level. This localized pressure perturbation leads to an enhanced pressure gradient toward the cooling layer as seen in the middle panel in Figure 12. The gravity also increases due to increased density (Fig. 12, *right panel*), but this is not large enough to compensate for the increased pressure gradient at this stage. This is seen by comparing the contours in the middle and right panels.

As a result, the upward acceleration is enhanced in the upflow immediately beneath the cooling layer, and the upflow velocity in the cooling layer increases.[5] This was also noted in the velocity curves for the low-viscosity events in Figure 2.

Next, we consider the development after $t = -2.0$ minutes, just before the collapse. The fluctuations in pressure, pressure gradient and buoyancy force at three depths, 0.3, 0.4, and 0.5 Mm, are shown in Figures 14 and 15. They are calculated from equation (9) with the time-averaged values subtracted (thereby eliminating the constants of integration), and dividing by the time averaged total pressure, e.g., $(P_{\text{adiab.}} - \langle P_{\text{adiab.}}\rangle)/\langle P_{\text{Total}}\rangle$.

At $z = -0.29$ Mm, the pressure is kept approximately constant up to $t = 0.0$ minutes. The adiabatic pressure increases due to the horizontal mass flux convergence. This is almost cancelled by a drop in nonadiabatic pressure. This effect is also seen in deeper at $z = -0.41$ Mm, with a growing adiabatic, and a decreasing nonadiabatic contribution. Hence, the pressure gradient between these two levels is kept roughly constant. Gravity eventually becomes larger than the total pressure gradient, as mass accumulates from neighbor granules. Downward acceleration follows, and upflow reverses to downflow.

To summarize: In the initial stages, the flow in the granule is upward. The flow at the surface is strongly accelerated downward, but the convective upflow below the surface is initially accelerated upward, due to incoming mass flux from neighboring, larger granules in subsurface layers. The process is akin to squeezing toothpaste from a tube. The situation just prior to granule collapse, is that the near-surface flow is still upward while the subsurface flow is downward, and mass is supplied by horizontal flow from surrounding granules.

The granule collapses at $t = 0.0$ minutes after the acceleration turns to downward everywhere (at about $t = -1.0$ minutes), when the adiabatic growth of the pressure gradient is counteracted by the combined effect of (1) radiative diffusion out of the relatively small granule fragment and (2)

[4] The specific entropy s decreases with height in the cooling layer (convective instability) and increases with height in the overlying atmosphere (convectively stable). The heat advection is therefore negative for upward motion in the stable atmosphere.

[5] This is opposite to "buoyancy braking" of the upflow in large, expanding granules, in which the positive pressure perturbation in the surface lowers the vertical pressure gradient, and brakes the upflow. In the current case, "buoyancy acceleration" occurs above a positive pressure perturbation in deeper layers.

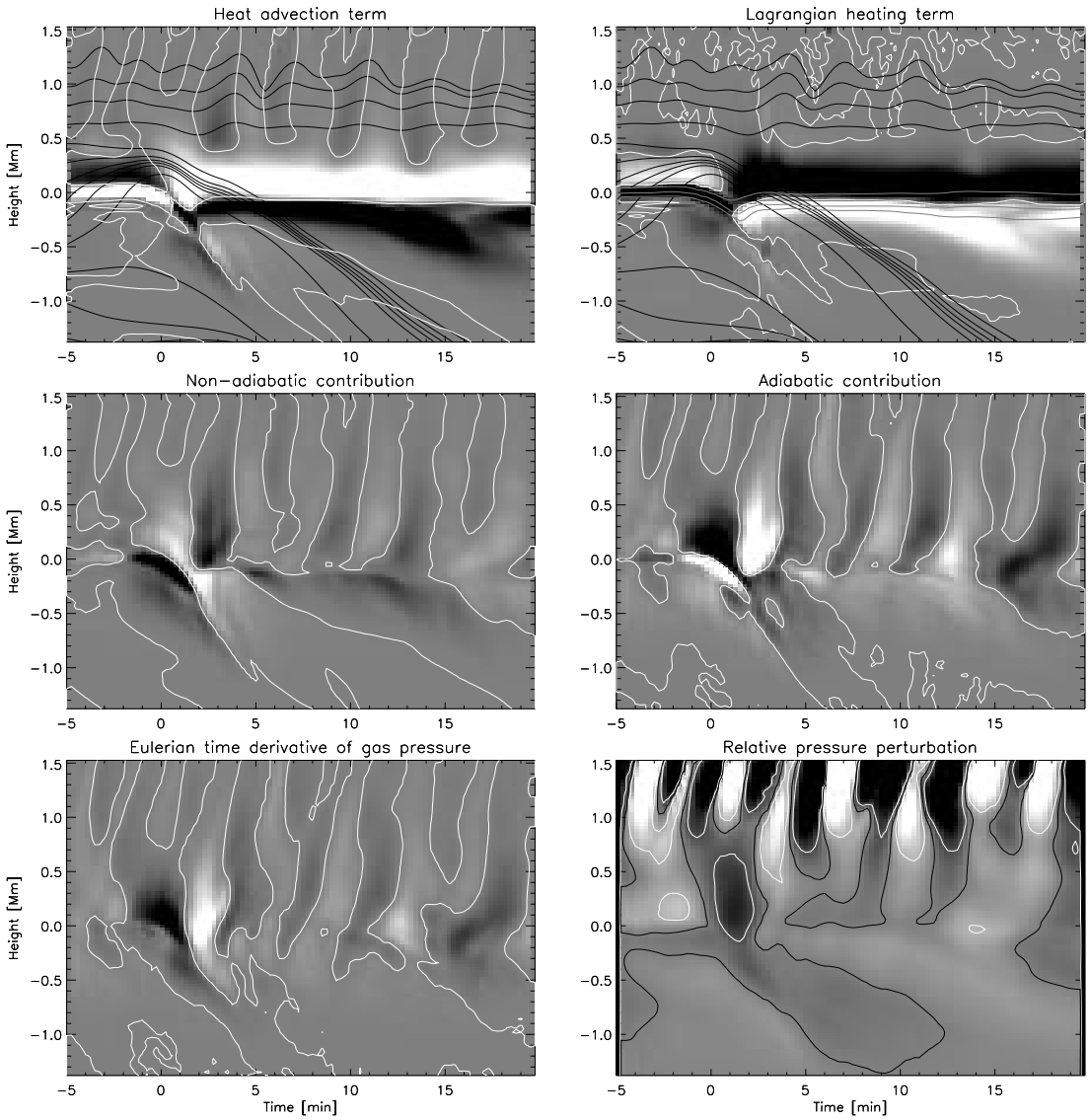

FIG. 9.—Contributions to pressure changes, event (B). All panels show the time evolution along the column centered on the event. The sum of the heat advection term (*upper left panel*) and the contribution from radiative energy exchange and viscous heating (*upper right panel*) is the rate of change of pressure due to nonadiabatic sources (*middle left panel*). The adiabatic contribution is in the middle right panel. The sum of the contributions in the middle panels is the total rate of change of pressure $\partial P/\partial t$ (*lower left panel*). The white contours in these figures mark the zero level. The black contours in the upper two panels are particle paths obtained from time integration of the vertical velocity. These are shown to indicate the direction of heat advection. The gray, mostly horizontal contours in the upper right panel are the levels of vertical optical depths of $\tau = 1$, 10, 50. The contours show the vertical displacements of the cooling layer. The lower right panel is the relative pressure perturbation (relative to the time average at each height). The black contours show zero perturbation, and the white contours show $\pm 20\%$ perturbations. All of the quantities, except for the relative pressure perturbation, are arbitrarily scaled with e^{6z} to show variations at a large height range. The pressure is mainly controlled by adiabatic changes in the atmosphere. The nonadiabatic changes are in antiphase with the adiabatic changes and serve to damp the adiabatic effect on the total pressure changes.

mixing of low entropy gas from the surrounding downdraft into the granule fragment (Figs. 14 and 15).

An important observational signature is that collapsing granules become brighter just before they collapse due to the enhanced upward enthalpy flux but leave behind an extended dark region in the vertex of the remaining granules.

Note also that the collapse is initiated in subsurface layers (not in the surface cooling layer) by a density increase due to a converging horizontal flow, which increases the downward buoyancy force, making it larger than the upward pressure gradient force. If, in contrast, the collapse was initiated in the surface by radiative overcooling, we would expect monotonically decreasing upflow velocity as in the central parts of an "exploding" granule.

5. WAVE EXCITATION

In response to the reversal from upflow to downflow in the collapsing granule, the fluid in the upper atmosphere is initially accelerated downward and then upward, which produces a rarefaction followed by a compression and then a decaying oscillatory wake (Figs. 10 and 11). The black contours mark locations of zero vertical acceleration separating the regions of positive (upward) and negative (downward) acceleration. The rarefaction and subsequent compression are nearly in phase (evanescent waves) in the photosphere and low chromosphere ($z \approx 0$–0.8 Mm), because their wavelength is larger than the atmospheric scale height. As the temperature increases in the middle and high chromosphere the scale height increases ($\propto T$) faster

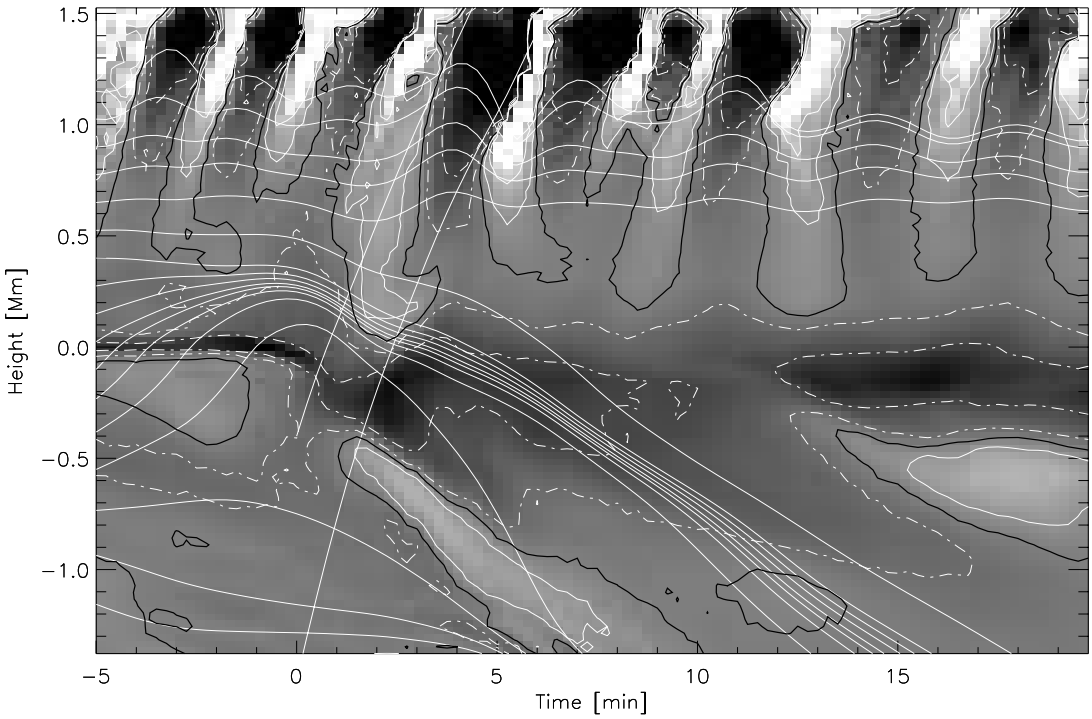

FIG. 10.—Vertical acceleration, event (B). Vertical acceleration as a function of time along the vertical column centered on event (B). Upward acceleration corresponds to lighter shades of gray, and downward acceleration to darker shades. Zero acceleration is marked by black contours. White dashed contours mark -20 and -60 km s^{-2} (downward) accelerations, and white solid contours $+20$ and $+60$ km s^{-2} (upward) accelerations. The white, mostly horizontal lines are particle paths obtained by time integration of the vertical velocity along the column. These have curvatures corresponding to the acceleration, as long as the horizontal velocity is negligible. The two slanted white lines that start at $t = 0.0$ and cover the full height range indicate the sound velocity. The flow reversal in the cooling layer occurs at $t = 0.0$ minutes. The downward-moving structure in the convection zone is a signature of a plume, while the skewed contours in the atmosphere are wave fronts of gravity modified acoustic waves. Supersonic wave propagation is seen in the chromosphere (faster than the sound velocity line) at about $t = 5$ minutes and $z > 1.2$ Mm, due to a vertically propagating shock.

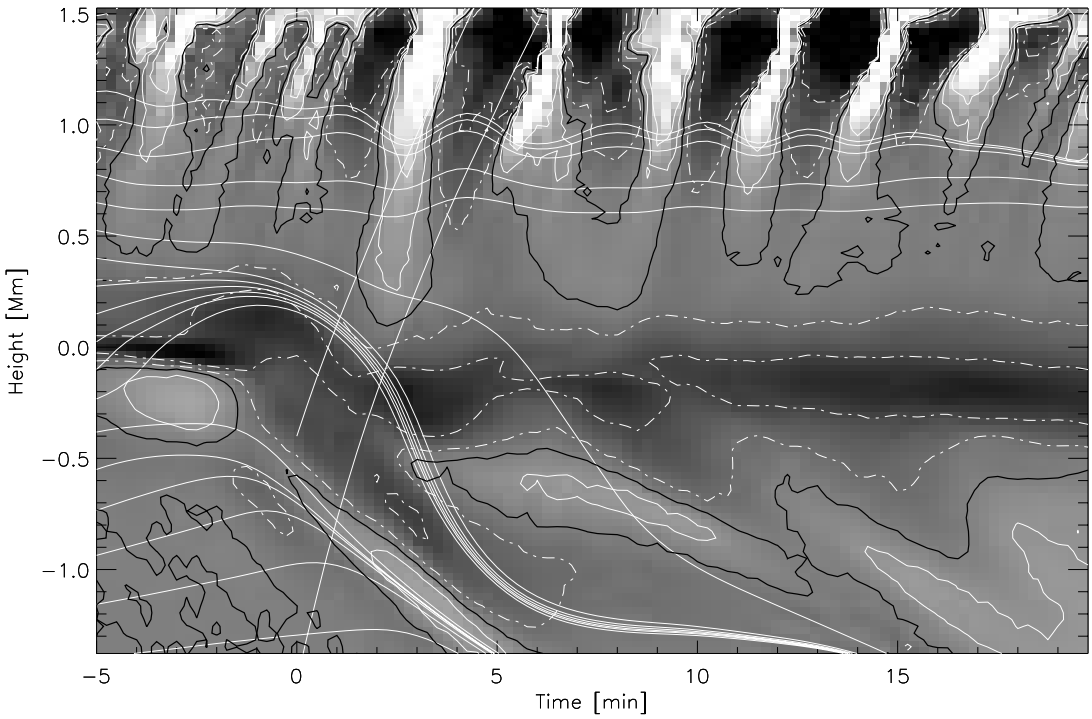

FIG. 11.—Vertical acceleration, event (A). Vertical acceleration as function of time along the vertical column centered on event (A). The contours, curves and image have the same meaning as in Fig. 10. In this case, and in contrast to event (B), the atmospheric oscillation prior to the excitation is less coherent and has less influence on the amplitude of the transient. The atmospheric response is in spite of this, similar to that of event (B). Note also the upward acceleration around $t = 2.0$ minutes that extends down to 100 km above the surface and into the region of wave excitation, as for event (B).

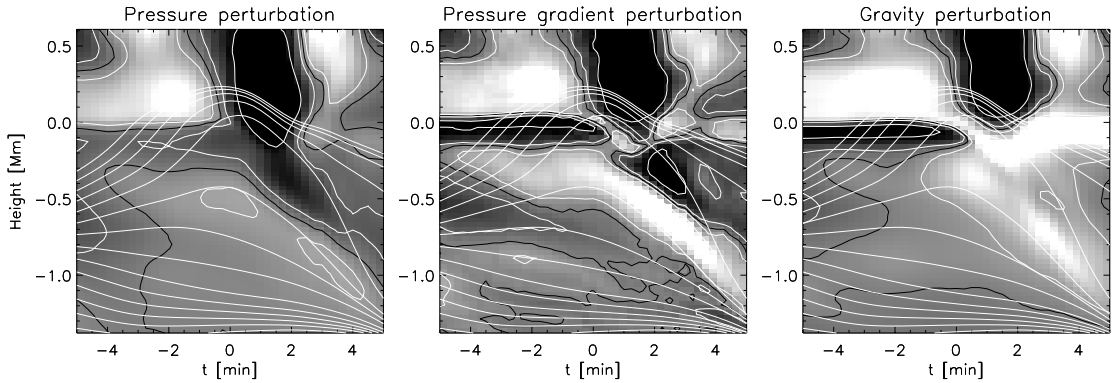

FIG. 12.—Relative perturbations in pressure, vertical pressure gradient and buoyancy force for event (B). The panels show $P/\langle P\rangle - 1$ (*left*), $(\partial P/\partial z)/\langle \partial P/\partial z\rangle - 1$ (*center*), and $(g\rho)/\langle \partial P/\partial z\rangle - 1$ (*right*), where the brackets denote time averaging. The buoyancy force is normalized with the average pressure gradient, so that the figures can be compared directly in the sense that higher value of the pressure gradient perturbation than the gravity perturbation gives a net upward force. White indicates enhanced upward and black enhanced downward pressure gradient force and vice versa for buoyancy. The black contour shows zero perturbations and the white contours, $\pm 5\%$ and $\pm 20\%$ perturbations. The particle paths for vertical motion are also shown. The relative pressure perturbation (*left panel*) increases in time in subsurface layers partially due to mass flux convergence from overturning fluid from neighboring upflow. This raises the pressure gradient (*middle panel*) toward the surface above $z = -0.7$ Mm, and serves to increase the upflow velocity in the cooling layer. Diverging particle paths correspond to vertical mass flux divergence, and this is slightly overcompensated by the horizontal mass flux convergence. Therefore, the gravity increases (*right panel*), but that is not sufficient to compensate for the raised pressure gradient close to the surface, until about $t = -1.0$ minutes. The pressure gradient and gravity images with contours are directly comparable since the gravity has been normalized the same way as the pressure gradient.

than their wavelength ($\propto T^{1/2}$). Only in the chromosphere above 1 Mm are the waves clearly propagating as shown by the slanted acceleration contours (at slightly supersonic speed, as can be seen in comparison with the two slanted white lines starting at $t = 0.0$ minutes which show a sonic path). Note that the upward acceleration region only extends down to the cooling layer, showing that the waves are excited in the photospheric overshoot region, not in the convection zone.

5.1. *Dynamics in the Photosphere*

This dynamical behavior can be understood by looking at the pressure and buoyancy forces (Figs. 12 and 13). The pressure changes are primarily adiabatic. Nonadiabatic effects act in the opposite sense to the adiabatic variations but are smaller. The pressure above the collapsed granule initially drops because the upflow changes to a downflow and the density is reduced.

Just prior to, and following the granule collapse [$t = (-1.5, 1.5)$ minutes], the density in the overshoot zone decreases (Fig. 13). This is initially due to divergent horizontal overshoot flow exceeding the vertical mass flux convergence (granular upflow). When the granule collapses and the downdraft forms (around $t = 0.0$ minutes), due to removal of the underlying pressure support (§ 4.3), the vertical mass flux becomes divergent and the density decreases. The resulting pressure deficiency (lower pressure than the surroundings) produces a horizontal pressure gradient that brakes the horizontal outflow. The horizontal flow becomes convergent (at about $t = 1.0$ minutes), but it is small until the adiabatically produced pressure gradient can accelerate the fluid toward the downflow. Hence, the density above the downflow decreases and continues to adiabatically reduce the pressure locally (Figs. 13, 12, and 9). The delayed response of the horizontal flow to the decreasing pressure is due to fluid inertia. Eventually (at about $t = 1.5$ minutes), the horizontal mass flux convergence overcompensates the vertical divergence, and the density in the overshoot layer above the downdraft increases again (Fig. 13). The density and therefore the pressure continue to increase, due to continued excessive horizontal mass flux convergence, and a pressure maximum relative to the surroundings at the same height builds up (Figs. 12 and 9).

This behavior can be viewed in a different way by studying a sequence of vertical slices through the acoustic event as a function of time (Figs. 16 and 17). Prior to granule collapse ($t = -2.0$ minutes) the convective upflow is seen as a vertical "tongue" in the white zero vertical velocity contour at about $y = 4.0$ Mm (Fig. 16, *upper left panel*). A downflow, originating from an intergranular lane, is deflected sideways into the deeper parts of the upflow at about $z = -1.0$ Mm. When the granule collapses and the associated upflow vanishes, the pressure decreases locally in the convective overshoot zone between $z = 0.0$ Mm and $z = 0.5$ Mm (Fig. 16, $t = 0.0$ minutes and $t = 1.25$ minutes). This pressure deficiency sets up horizontal pressure gradients, that accelerate the flow horizontally toward the site of collapse, and horizontal mass flux convergence is initiated. The pressure increases due to this inflow (Fig. 17, $t = 2.91$ minutes) and reaches a maximum around 3 minutes.

A stagnation point (upflow above and downflow below) develops at about $y = 3.7$ Mm, $z = 0.2$ Mm and $t = 2.91$ minutes. The upward velocity at $z = 0.7$ Mm is now maximum, with a corresponding pressure maximum, as in a propagating acoustic wave. This locally enhanced pressure produces a horizontal expansion and horizontal wave components at $t = 4.16$ minutes, between $z = 0.5$ Mm and $z = 1.0$ Mm. As the positive pressure perturbation propagates horizontally outward in both directions, the pressure at the site of the initial perturbation decreases. This is seen as the "flattened doughnut" centered at $y = 3.8$ Mm, $z = 0.8$ Mm. The horizontal propagation continues at $t = 5.41$ minutes and $t = 5.83$ minutes. It is this wave that appears as a horizontally expanding circular ring in vertical velocity (see the observers view in Fig. 1 at coordinates (4.0,

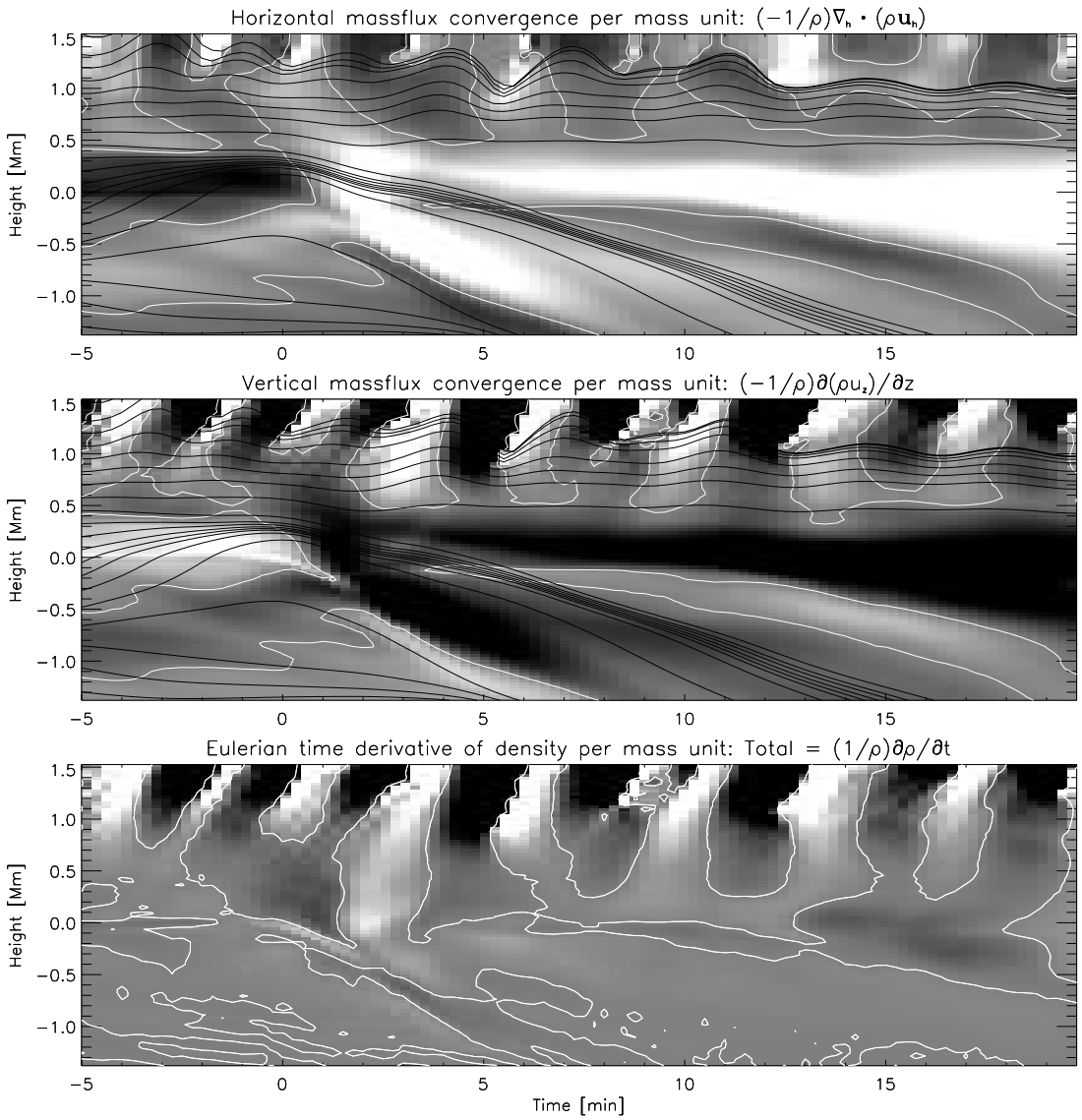

FIG. 13.—Mass conservation, event (B). The images show the time evolution along the vertical column centered on the event, of horizontal (*upper panel*) and vertical (*middle panel*) mass flux convergence, normalized by density. The lower panel shows the sum of these contributions, which is the relative rate of change of density. The time axis shows elapsed time in minutes after downward motion starts in the granule at $z = 0.0$ Mm. White contours mark zero mass flux divergence and zero rate of change of density. The black lines are particle paths corresponding to vertical velocity along the column.

0.5) and $t = [2.5–4.5]$ minutes). The density contours in the sequence display V-shaped, horizontally expanding phase fronts that correspond to a downward directed wavevector. These fronts are seen by drawing a line through the peaks of adjacent density contours. The horizontal and vertical components of the wavevector, together with an oscillation period of about 3 minutes, locate this wave mode in the gravity wave domain. The group velocity vector points away from the source location (in linear theory the group velocity roughly parallels the phase fronts and so is perpendicular to the wavevector). The wave period would have been considerably shorter than 3 minutes if these oscillations were acoustic with the same direction of the wavevector. The Brunt-Väisälä period is slightly lower than the acoustic cutoff period of 3 minutes, hence these wave components are barely within the gravity wave domain. Furthermore, they do not survive for more than 2–3 oscillation periods in the vicinity of the event before they are washed out by interaction with flow and other wave components. The wave amplitude is, in addition, damped by the geometrical effect of expansion.

At $t = 5.41$ minutes, gas flows downward to the negative pressure perturbation at $y = 3.8$ Mm and $z = 0.8$ Mm. The downward-moving gas falls into the relatively slow-moving gas at around $z = 0.8$ Mm, resulting in nonlinear steepening of an upward propagating wavefront at $z = 1.2$ Mm and $t = 5.83$ minutes. This wavefront becomes supersonic at a later stage and belongs to the family of gravity modified acoustic waves.

Still another way of visualizing the photospheric fluid flow following granule collapse is a sequence of three-dimensional fluid particle paths. Figure 18 shows fluid trajectories of 1.7 minutes duration at intervals of 2.5 minutes. The collapsing granule initiates a downdraft plume into the convection zone. This downflow at the site of the collapsing granule reduces the pressure in the overshoot zone, and atmospheric gas flows into the wake (Fig. 18, *upper left panel*). This is the rarefaction phase of the atmospheric

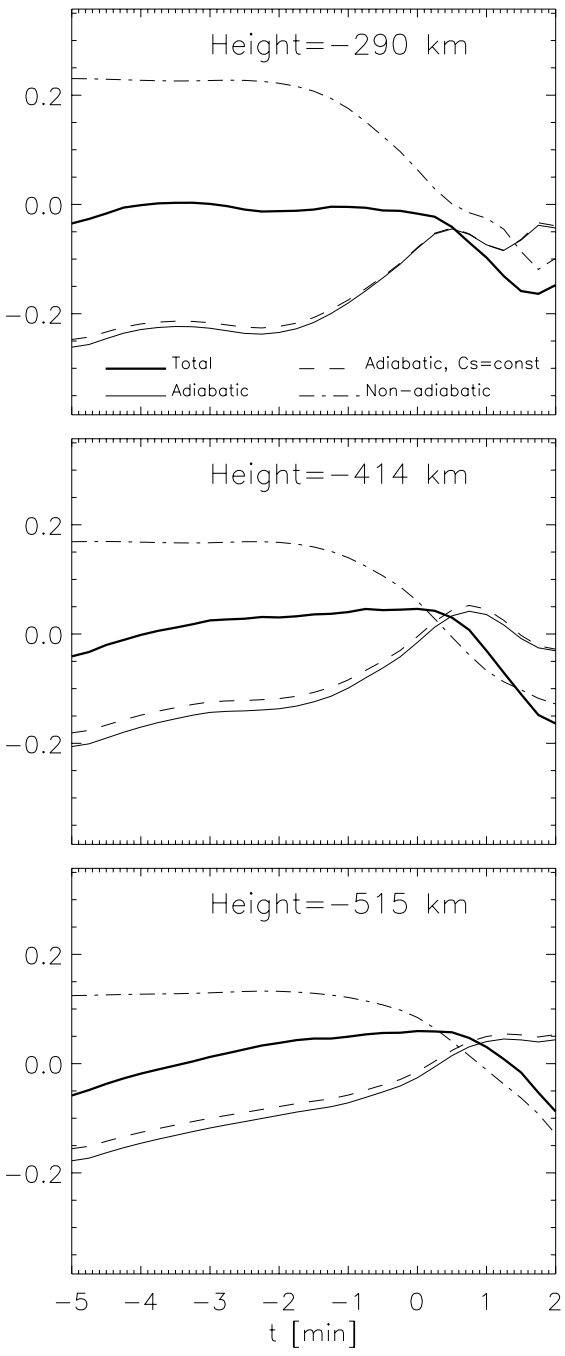

FIG. 14.—Pressure perturbations in the collapsing granule

wave. Most of the gas initially below about 0.5 Mm above the granule ends up in this plume, or in previous, nearby downdrafts. Eventually, the pressure is restored mainly by this horizontal mass inflow. Some gas overshoots vertically after the pressure has been restored (Fig. 18, *upper left panel*). This is the compression phase in the wave that has been launched.

Now, consider the effect in chromospheric layers (see Figs. 10 and 11). For event (B) between $z = 1.0$ Mm and $z = 1.5$ Mm, the first downward motion associated with the transient reverses abruptly back to upward motion. This is a vertically propagating shock wave, and its supersonic propagation speed can be seen by a comparison with the sound velocity curves. The particle paths between subsequent shocks are similar to parabolas due to free fall under the pull of gravity. Supersonic propagation and shock formation occurs also for event (A),[6] but in higher chromospheric layers at $t = 6.5$ minutes close to $z = 1.5$ Mm.

5.2. *Adiabatic versus Nonadiabatic Pressure Fluctuations in the Photosphere*

Figure 9 shows the adiabatic and nonadiabatic contributions to the pressure fluctuations as a function of time in a vertical column centered on Event B. Figure 19 shows the relative pressure fluctuations at two different levels in the overshoot zone, at $z = 200$ km and $z = 400$ km, and in the cooling layer at $z = 0.0$ km. The total pressure is split into an adiabatic part and a nonadiabatic part, and the fluctuations in these quantities relative to the total pressure are shown in the figure. The two pressure contributions are calculated by equation (8). Adiabatic fluctuations are shown by the thin solid line and nonadiabatic fluctuations by the thin dash-dotted line. The total pressure fluctuation is the sum of the two contributions and is shown by the solid, thick line.

At $z = 200$ km and $z = 400$ km, the total pressure fluctuation is mainly dominated by, and therefore in phase with, the adiabatic fluctuation. The nonadiabatic contribution is in antiphase with and smaller than the adiabatic fluctuation, so it decreases the amplitude of the total pressure fluctuation.

The squared sound velocity is essentially proportional to the temperature and can modulate the influence from the density changes. The dashed curve shows the adiabatic fluctuation that would result for constant sound velocity. We here used the time averaged sound velocity at the same levels. This curve is not radically different from the actual adiabatic fluctuation, and we can therefore conclude that the temperature modulation is not very important. This can be understood, since the photospheric gas is kept close to the radiation equilibrium temperature by radiative heating or cooling.

Hence, we can conclude that the pressure changes in the overshoot zone are mainly controlled by density changes and that their amplitude is damped by nonadiabatic effects.

We now explain the adiabatic and nonadiabatic pressure variations in more detail. Before the collapse, the overshoot flow at $z = 200$ km is radiatively heated and adiabatically cooled (see Fig. 9). The negative heat advection due to the upward velocity (since specific entropy increases upward in the photosphere) is almost in balance by the radiative heating, and the net effect is adiabatic cooling (due to expansion). After $t = 0.0$ minutes, the downflow has started, and the heat advection becomes positive. This is undercompensated by radiative cooling, so there is a nonadiabatic pressure increase in time. This is the reason for the

[6] For event (B), we see relatively small amplitude oscillations in atmospheric layers with a dominating period of about 2.0 minutes before the transient is excited. It appears from the figure that the upward acceleration of this oscillation is approximately in phase with the upward acceleration from the wave excitation. This serves to amplify the displacements and vertical velocity of the wave transient. This effect is not present or is much weaker for event (A), for which the atmospheric oscillation prior to the excitation is less coherent and has smaller amplitude. The atmospheric response for event (B) is, in spite of the extra contribution from interference, qualitatively the same as for event (A).

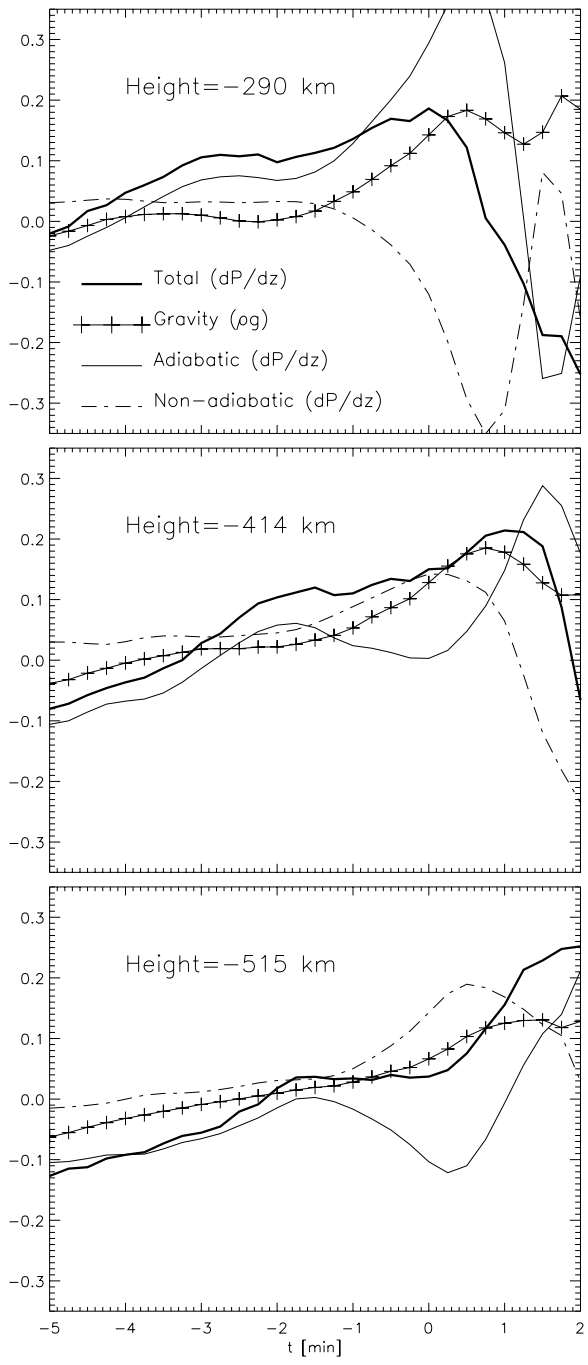

FIG. 15.—Pressure gradient perturbations and gravity in the collapsing granule.

increasing nonadiabatic contribution in Figure 19. After $t = 2.0$ minutes, radiative cooling is larger than the positive heat advection, and the nonadiabatic contribution to the pressure decreases. This is the reason for the decreasing nonadiabatic contribution in Figure 19. In higher layers at $z = 400$ km, the nonadiabatic contribution is mainly due to the vertical heat advection, with increasing (decreasing) nonadiabatic pressure for the downward (upward) moving phases. Radiative cooling is in antiphase, and serves to damp the advection effect.

We now discuss the cause of the pressure variations at the base of the photosphere, in the radiative cooling layer. This is of interest, since thermodynamic acoustic sources set up by radiative cooling in this layer may be important, as indicated by the simulations of Rast (1999).

There is a large positive contribution from upward heat advection in the cooling layer (Fig. 9, $z = 0.0$ km). This is almost balanced by radiative cooling, but initially, there is some net heating and increasing nonadiabatic pressure, due to the increasing upflow velocity just before the collapse. The increasing nonadiabatic pressure is almost cancelled by a negative contribution from decreasing density (see also Fig. 19, *bottom panel*), and the total pressure remains almost constant. The cooling layer therefore expands isobarically due to net heat input, before the granule collapses.

At about $t = -2.0$ minutes, the reduced upward heat advection is not sufficient to balance the radiative cooling, and the nonadiabatic pressure decreases. This is again compensated by the adiabatic contribution that is positive, due to increasing density. This is isobaric contraction due to net heat loss.

Due to this cancellation effect, the total pressure remains approximately constant in the cooling layer until granule collapse at $t = 0.0$ minutes. The pressure variations are small and slow ($\sim 10\%$ in 5 minutes), prior to the flow reversal in the granule (Fig. 19, *bottom panel*). A negative pressure perturbation ($\sim -30\%$) occurs after the flow reversal, primarily due to adiabatic changes. The pressure first decreases due mainly to adiabatic expansion in the downdraft, and then it increases due to the following compression. We therefore conclude that, for the collapsing granule case, the pressure changes that contribute to wave excitation in the cooling layer are not thermodynamic in origin, but due to imbalance between vertical and horizontal mass flux divergence.

The actual forces, of course, are due to the pressure gradient and buoyancy. Figure 20 shows the relative fluctuation in the pressure gradient, $(dP/dz - \langle dP/dz \rangle)/\langle dP/dz \rangle$, and the normalized fluctuation in gravity, $(g\rho - \langle dP/dz \rangle)/\langle dP/dz \rangle$. The normalization factor is the time averaged pressure gradient at the given height. The contributions from adiabatic and nonadiabatic pressure gradients are also shown in the figure. These contributions are given by a time integration of equation (10), and normalized such that their sum is equal to the relative fluctuation in the total pressure gradient.

The adiabatic pressure gradient falls faster than the gravity in the phase of downward acceleration (where the gravity is larger than the total pressure gradient). Later, in the phase of positive acceleration, the adiabatic pressure gradient rises faster than the gravity. By using the adiabatic part of equation (10), we can write this effect as

$$g \left| \frac{\partial \rho}{\partial t} \right| < \left| \frac{\partial}{\partial z} \left\{ c_s^2 \frac{\partial \rho}{\partial t} \right\} \right| = \left| \frac{\partial}{\partial z} \{ c_s^2 \nabla \cdot (\rho \boldsymbol{u}) \} \right| . \quad (11)$$

From the density perturbations in Figure 13, we see that for a change $\delta\rho$ in time, $\delta\rho/\rho \sim$ const. in the height direction in the overshoot zone. We can therefore write $\delta\rho \sim e^{-z/H}$, since the density varies approximately exponentially with height. H is the density scale height. We can then write the last equation as (setting the sound velocity to a constant, typical value):

$$g\,|\,\delta\rho\,| < \left| \frac{c_0^2}{H}\,\delta\rho \right| . \quad (12)$$

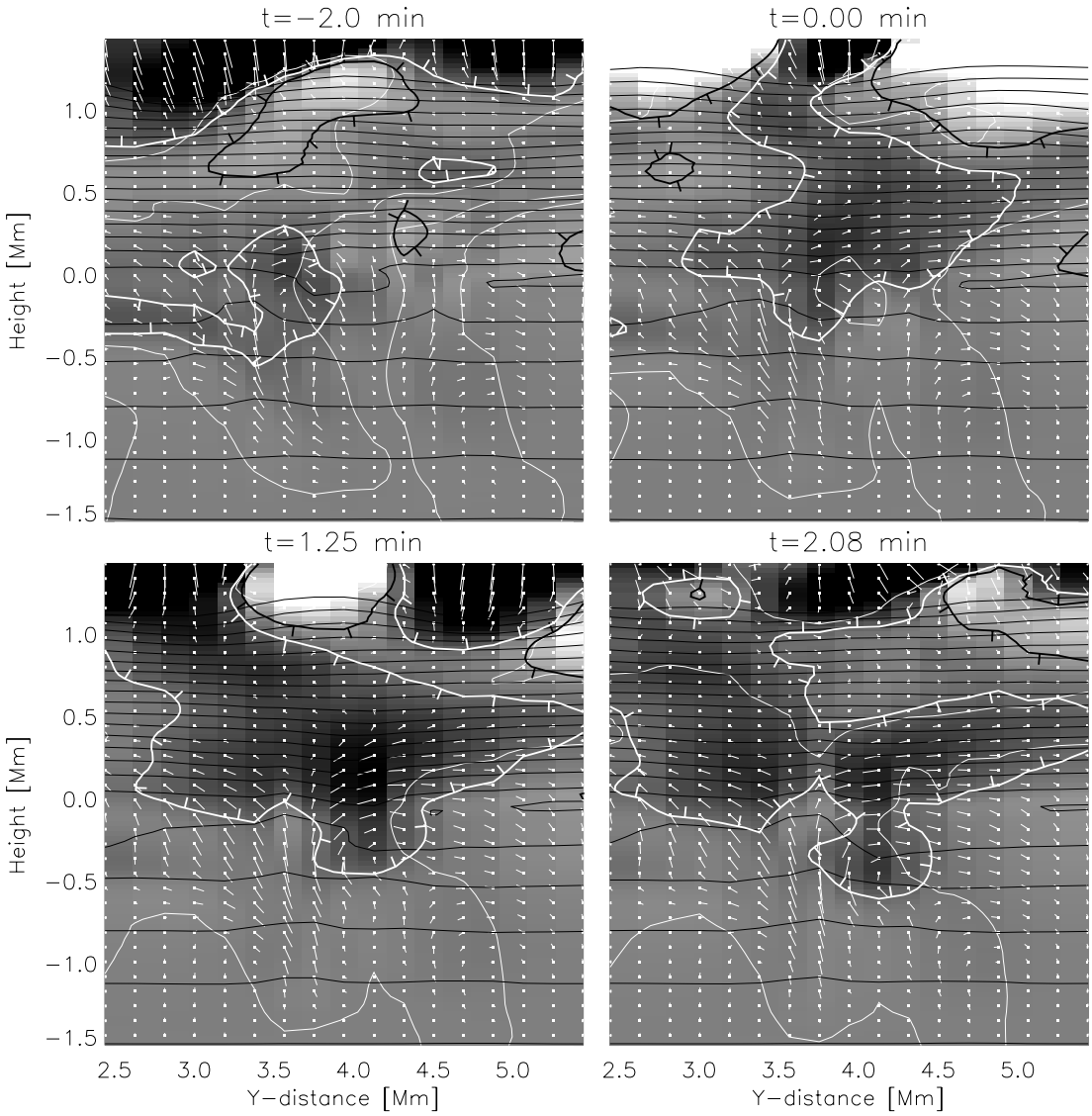

FIG. 16.—Cell collapse and photospheric pressure perturbation, event (B). Shaded picture: relative pressure perturbation from the mean pressure. Black and white contours: +10% and −10% pressure perturbations, respectively. The ticks on these contours point in the downhill direction (away from the positive pressure gradient perturbation). Black contours are density contours. White contours: zero vertical velocity. The zero velocity contour encloses the vanishing cell as a vertical "tongue" at about $y = 4.0$ Mm in the upper left panel ($t = -2.0$ minutes). A downflow, originating from an intergranular lane, is deflected sideways into the deeper parts of the collapsing cell at about $z = -1.0$ Mm. As the cell collapses, the pressure decreases locally between $z = 0.0$ Mm and $z = 0.5$ Mm. This generates horizontal pressure gradients that accelerate the flow horizontally toward the site of collapse, and a horizontal mass flux convergence is initiated ($t = 0.0$ minutes). The pressure builds up due to the horizontal mass flux convergence ($t = 2.08$ minutes). The pressure support of the overlying atmosphere is reduced by the negative pressure perturbation between $z = 0.0$ Mm and $z = 0.5$ Mm, such that a downflow is initiated. This is reversed to upflow when the pressure increases ($t = 2.08$ minutes).

The ratio of the two sides is the Froude number[7] $F_r = c_0^2/H/g > 1$. In the current case for the overshoot zone, $F_r \sim 2$, using typical values in this layer. Hence, the rate of change of the adiabatic pressure gradient is only marginally larger than the rate of change of gravity.

The change in the total pressure gradient is also influenced by the nonadiabatic contribution in equation (10):

$$\frac{\partial}{\partial z}\left\{(\Gamma_3 - 1)\rho T \frac{\partial s}{\partial t}\right\}.$$

For the purpose of demonstration, we assume that a change in time of heat, $\delta q = T\delta s$, is constant with height.[8] We also set Γ_3 constant with height, which is a good approximation in the overshoot zone. The nonadiabatic contribution now becomes, with $\rho \sim e^{-z/H}$,

$$(\Gamma_3 - 1)\frac{\delta Q}{H}, \tag{13}$$

[7] The Froude number is also the typical ratio (inertial term)/(gravity term) in the equation of motion.

[8] This approximation is valid when the advection part includes a linear variation of s with height (which is a good approximation), and constant vertical velocity. We must also assume constant specific radiative heating with height.

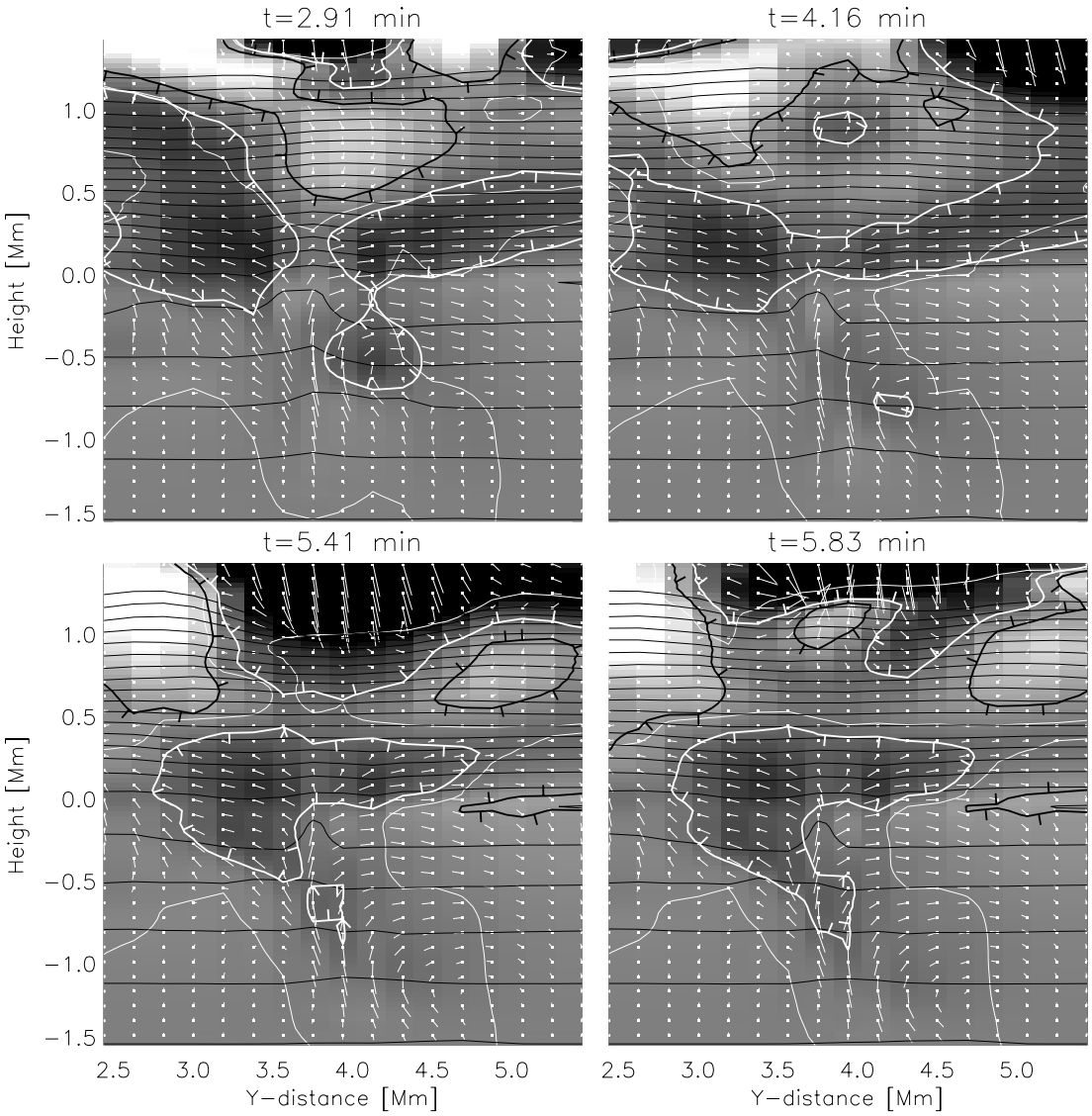

FIG. 17.—Photospheric pressure perturbation and wave excitation, event (B). For the coding, see the previous Fig. 16. At $t = 2.91$ minutes, the pressure immediately above the downflow is still increasing, and a stagnation point has developed at about $y = 3.7$ Mm, $z = 0.2$ Mm. The upward velocity at $z = 0.7$ Mm is now maximum, with a corresponding pressure maximum, as in a propagating acoustic wave. At $t = 4.16$ minutes, this pressure maximum has induced horizontal outflow and corresponding mass flux divergence, with accompanying pressure decrease, as seen as the "flattened doughnut" centered at $y = 3.8$ Mm, $z = 0.8$ Mm. A horizontal wave component has now been induced. At $t = 5.41$ minutes, gas flows toward this pressure minimum from the sides and from above. The downward-moving gas falls into the relatively slow-moving gas at around $z = 0.8$ Mm, resulting in nonlinear steepening of an upward propagating wavefront (develops to a shock) at $z = 1.2$ Mm and $t = 5.83$ minutes. Here we also see the horizontally propagating pressure perturbation, accompanied by raised density contours. This is a pressure modified gravity wave which is driven by buoyancy and horizontal pressure gradients.

for a change of heat per volume unit δQ (ergs cm^{-3})

$$\delta Q = \rho \delta q = \rho(q_{\text{rad.}} + q_{\text{visc.}} - \boldsymbol{u} \cdot T \nabla s) \, . \tag{14}$$

This example shows that the pressure gradient increases by radiative and viscous heating and/or positive heat advection by downward motion in the atmosphere.

Gathering all contributions, we can now write, using equation (3), an approximate equation for the perturbation in the vertical force:

$$\delta F_z \sim \left\{ \frac{c_0^2}{H} - g \right\} \delta \rho + (\Gamma_3 - 1) \frac{\delta Q}{H} \, . \tag{15}$$

In the initial stages of the wave excitation, the acceleration is driven by changes in the buoyancy force and adiabatic changes in the pressure gradient (first term). The nonadiabatic contribution to the pressure gradient (second term), is in antiphase with the adiabatic contribution, just as for the pressure fluctuations. The actual contributions to this force balance are seen in Figure 20.

5.3. *Excitation of Acoustic Events*

The fluid in the atmosphere is initially accelerated downward and then upward, which produces a rarefaction followed by a compression and then a decaying oscillation (Figs. 10 and 11). We now consider the details in the vertical force balance to explain this wave excitation. Consider Figure 20. Downward acceleration is initiated at 400 km ($t = -1.5$ minutes) by a reduction in the adiabatic pressure gradient. As the density declines due to reduced vertical

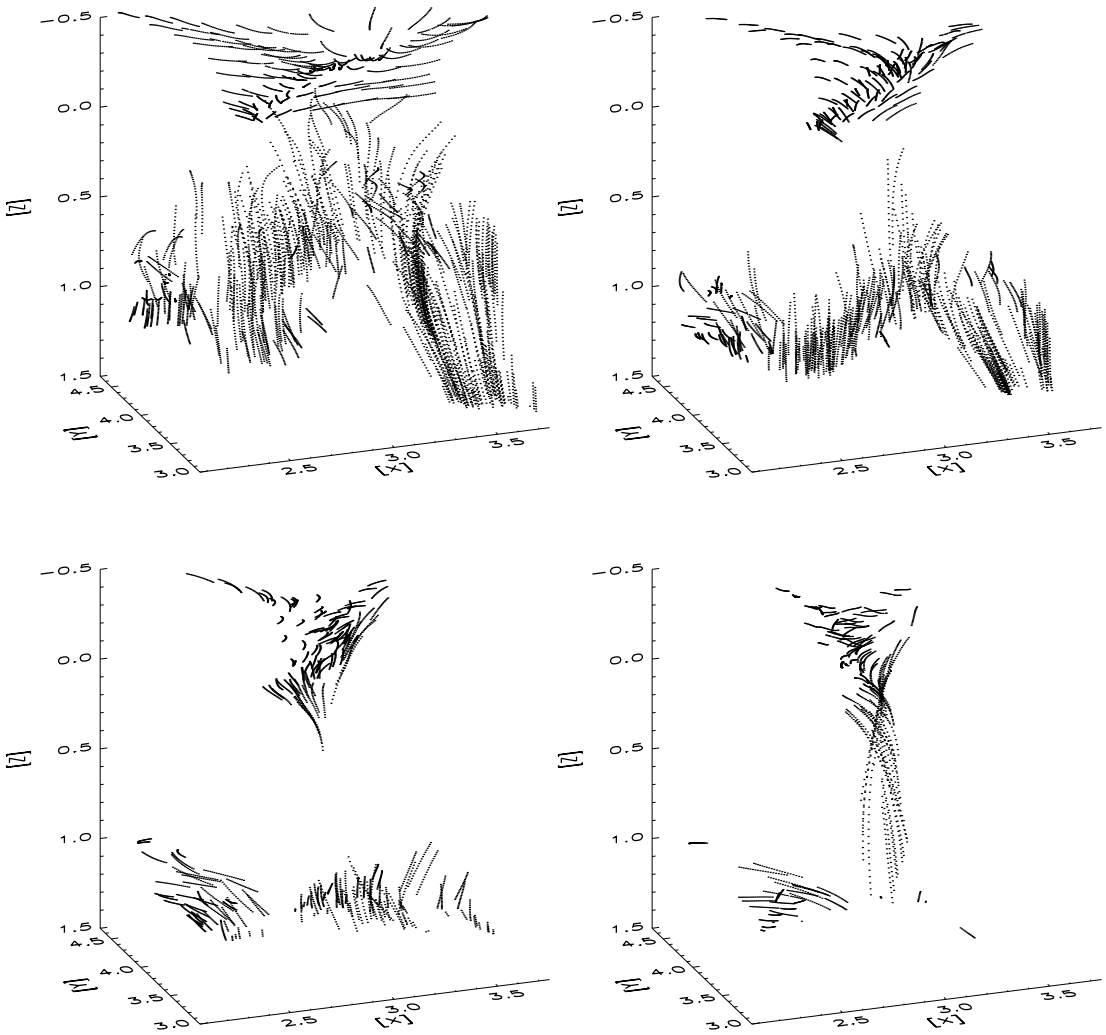

FIG. 18.—Fluid parcel trajectories. The paths are for fluid initially located above 0.4 Mm. The paths have 1.7 minute duration, with starting times are 2.5 minutes apart. The time series is started immediately after granule collapse (*upper left panel*) and ends where the two subsurface downflows (the two "legs") merge to form a stronger downflow (*lower right panel*). Note that all of the gas in shallower layers ends up in this downflow. The upper left panel shows the mainly horizontal inflow of atmospheric gas toward the pressure minimum that has developed (at −0.5 Mm). Some of the atmospheric gas ends up into the deeper downdraft as seen in the bottom right panel.

mass flux convergence (and sustained horizontal divergence), the pressure gradient falls adiabatically, and at a higher rate than the gravity. The nonadiabatic modification contributes little to the total pressure gradient in the initial phase, and downward acceleration results.

The downward acceleration initiates downward velocity and an increase in the nonadiabatic pressure gradient, due to positive heat advection. This is because the specific entropy increases in the upward direction in the photosphere. This damps the influence from the decreasing adiabatic pressure gradient. At $t = 1.5$ minutes, the positive contribution from the nonadiabatic pressure gradient serves to raise the total pressure gradient above the gravity, and upward acceleration starts. This produces a compression pulse following the rarefaction wave.

Immediately afterward, the photospheric downflow reverses to upflow, and the contribution from the nonadiabatic pressure gradient decreases, due to negative heat advection. In spite of this, the total pressure gradient continues to increase because the rise in the adiabatic pressure gradient overcomes the fall in the nonadiabatic pressure gradient. The adiabatic pressure gradient is rising due to excess horizontal mass flux convergence. The rate of change in the adiabatic pressure gradient is again larger than the rate of change in gravity.

Maximum upward velocity is reached at 400 km and above, when downward acceleration eventually sets in again (Fig. 10). The atmosphere continues to oscillate vertically, with a period close to the cutoff period of 3 minutes.

The fluctuations in pressure gradient and gravity for 200 km are qualitatively the same as for 400 km in the stages of wave excitation ($t = -1.5$ minutes to $t = 3.0$

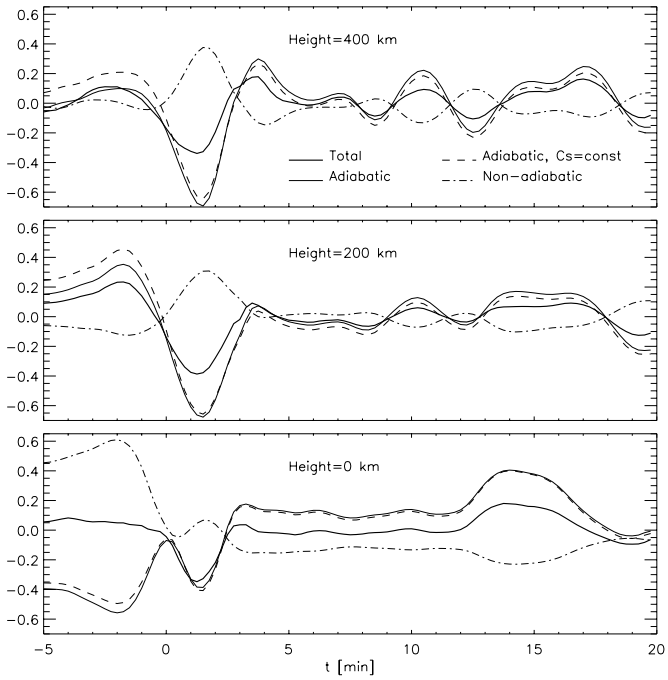

FIG. 19.—Pressure perturbations in the overshoot zone, event (B). These perturbations are given by the difference between the actual pressures and the corresponding time averages and divided by the total time averaged pressure. The total pressure perturbation is the sum of adiabatic and nonadiabatic contributions. The actual adiabatic pressure perturbation does not deviate very much from the adiabatic pressure fluctuation resulting from a constant sound velocity (essentially temperature). The total pressure perturbation is mainly controlled by the adiabatic fluctuation, but the amplitude is lower than the adiabatic fluctuation, due to nonadiabatic damping. The lower panel shows the perturbations in the cooling layer. All perturbations are measured directly above the collapsing granule (actually within it at 0.0 km).

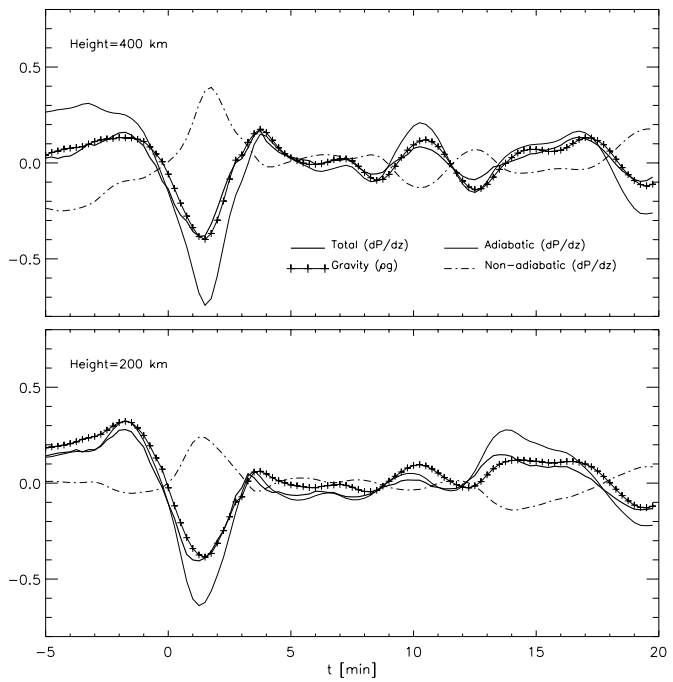

FIG. 20.—Vertical force balance in the overshoot zone, event (B). The perturbations in vertical pressure gradient and gravity have been normalized (see the text) by the time averaged pressure gradient at each height, such that when the gravity curve is larger than the pressure gradient, downward acceleration results. The sum of the adiabatic and nonadiabatic perturbations is equal to the total pressure gradient perturbation. Downward acceleration starts at 400 km just before the granule collapses at $t = 0.0$ minutes, mainly due to adiabatic reduction of the pressure gradient (caused by reduced density), which dominates over the corresponding reduction in gravity. The increasing nonadiabatic contribution (by positive downward heat advection) eventually raises the pressure gradient above the gravity, and upward acceleration starts. The adiabatic pressure gradient now increases (due to horizontal mass flux convergence) at a larger rate than the now decreasing nonadiabatic contribution (by negative upward heat advection), such that the upward acceleration continues. At 200 km, the pressure gradient is initially lower than the gravity due to balancing of upward decreasing vertical momentum flux in the convective flow.

minutes), as seen in Figure 20. The fluctuations in net vertical force are therefore also qualitatively the same, and caused by the same processes.[9]

The signature of wave excitation was seen for events (A) and (B) in Figures 11 and 10 (at $t \sim 2.0$ minutes), as a propagating region of upward acceleration from the lower photosphere and upward. The slanted contour which mark zero acceleration in the figures delineates this region and show upward acceleration down to $z = 0.1$ Mm. Below that level, the convective flow adds a negative acceleration component, but this is perturbed by a smaller upward acceleration during wave excitation. The contours which mark negative acceleration in the figures indicate that this perturbation extends down to the cooling layer.

[9] Before $t = -1.5$ minutes, we see that the 400 km curves show approximate hydrostatic equilibrium, while the 200 km curves do not. The gravity is somewhat larger than the pressure gradient for 200 km, with resulting net downward force. This is not a contribution to the wave excitation, but the contribution from momentum balance in the convective flow prior to the collapse. This contribution is stronger at heights closer to the cooling layer. In steady state (slowly evolving convective flow prior to cell collapse), and assuming that horizontal velocities are small, we can write this contribution as

$$\rho \frac{\partial}{\partial z}\left\{\frac{1}{2} u_z^2\right\} = -\frac{\partial P}{\partial z} - g\rho < 0 \,. \tag{16}$$

The inequality sign stems from the fact that the magnitude of the vertical velocity is decreasing with height in both upflows and downdrafts in the normal, slowly evolving convective overshoot flow.

If the wave source was located in the convection zone, we would have seen this perturbation also in deeper layers. We therefore conclude that the wave source is not located in the convection zone, but in the convective overshoot zone (from the cooling layer at $z = 0.0$ Mm and to about 0.5 Mm above).

Upward propagating waves (*slanted contours*) are evidently present in the oscillating wake that follows the acoustic event. Approximately one half wavelength, or even less, fits within the interval [0.3,1.5] Mm up to the upper boundary. The 3 minute period is present in both events, as also shown previously. These long wavelengths indicate strongly gravity modified acoustic waves, as is expected for oscillation periods close to the cutoff period. The oscillations have an evanescent character below $z = 0.5$ Mm and are visible in the figures down to $z = 0.3$ Mm (as sign changes in the acceleration).

6. SUMMARY

Acoustic events are produced when relatively small granules collapse, with the granular upflow turning into downflow, on a timescale shorter than the 3 minute acoustic cutoff period of the atmosphere. Granular collapse is pro-

duced by (1) starving the granule for energy because it lies above or near a mesogranule boundary downflow and (2) squeezing the granule by expansion of surrounding granules (with greater energy flow) and the tendency for downflows surrounding a small granule to merge.

Reversal of upflow to downflow produces an adiabatic decrease in the pressure (diverging mass flux) in the convective overshoot flow in the lower photosphere. This pressure drop excites an atmospheric rarefaction wave and alters the photospheric horizontal granular outflow to an inflow. The converging flow then adiabatically increases the pressure and produces a compression wave following the rarefaction. The acoustic waves that are excited are nearly evanescent vertically in the photosphere. They become vertically propagating in the chromosphere, steepen into shocks there, and leave behind a decaying oscillating wake, the first few waves of which may also steepen into shocks. Since the acoustic event is initiated by the formation of a downdraft, it is associated with a darkening in the intergranular lane. This process might therefore explain the observed "acoustic events" (Rimmele et al. 1995).

The excitation process is similar to the last stage in the three step excitation process modeled by Rast (1999), in which downflow initiates horizontal inflow and pressure recovery. However, in Rast's model, the downflow plume is produced by catastrophic local surface cooling (as occurs in the center of exploding granules), which is considerably different than excitation by a collapsing granule, which is primarily driven by subsurface dynamics.

There were seven acoustic events observed in the 65 minutes simulated, covering an area 36 Mm^2. This is equivalent to an occurrence rate of 3×10^{-3} events $minute^{-1}$ Mm^{-2}, which corresponds to approximately 2×10^4 events $minute^{-1}$ for the whole surface of the Sun. The wave excitation process described here plays an important role in the production of 3 minute atmospheric waves and the shock waves observed as "bright grains" in the Ca II H and K line cores. It must also be noted that collapsing granules might not be the only explanation for wave sources that produce bright grains and associated chromospheric shocks. The two-dimensional simulations of Steiner et al. (1998) show that a natural mechanism for the generation of vertically propagating shock waves can be provided by the interaction between flux sheets (flux tubes in three-dimensions) and convection.

Finally, we note that collapsing granules may also play a significant role in the excitation of *p*-modes via pressure fluctuations set up in the subsurface downflow plume resulting from the granule collapse (Stein & Nordlund 2000).

Andreas Botnen is thanked for his conversion of the new radiation part in the code to parallel versions running on different parallel computers. Mark Rast, Tom Bogdan, Teresa L. Palmer, Nick Hoekzema, Rob Rutten, Peter Brandt, and Mats Carlsson are thanked for illuminating discussions. Øyvind Andreassen at Forsvarets Forskningsinstitutt (FFI) in Norway, and the group at Colorado Research Associates (CoRA) in Boulder, USA, are thanked for providing efficient volume visualization tools, and for their scientific enthusiasm. R. S. received support from the Norwegian Research Council through a Ph.D. grant, through a grant of computing time (Program for supercomputing), and by grant 121076/420, "Modeling of Astrophysical Plasmas." Å. N. was supported by the Danish Research Foundation, through its establishment of the Theoretical Astrophysics Center. R. F. S. received partial support from NSF grants AST 9521785 and AST 9819799 and from NASA grants NAG 5-4031 and NAG 5-8053.

REFERENCES

Carlsson, M., & Stein, R. F. 1997, ApJ, 481, 500
Espagnet, O., Muller, R., Roudier, T., Mein, P., Mein, N., & Malherbe, J. M. 1996, A&A, 313, 297
Goldreich, P., & Kumar, P. 1990, ApJ, 363, 694
Gustafsson, B. 1973, Uppsala Astr. Obs. Ann., 5, 6
Gustafsson, B., Bell, R. A., Eriksson, K., & Nordlund, Å. 1975, A&A, 42, 407
Hirzberger, J., Bonet, J. A., Vasquez, M., & Hanslmeier, A. 1999, ApJ, 515, 441
Kalkofen, W., Rossi, P., Bodo, G., & Massaglia, S. 1992, in ASP Conf. Ser. 26, Cool Stars, Stellar Systems and the Sun, ed. M. Giampapa, J. M. Bookbinder (San Francisco: ASP), 543
Kato, S. 1966, ApJ, 144, 326
Lamb H. 1908, Proc. London Math. Soc., 7, 122
Lighthill, M. J. 1952, Proc. R. Soc. London A, 211, 564
Musielak, Z. E., Rosner, R., Stein, R. F., & Ulmschneider, P. 1994, ApJ, 423, 474
Nordlund, Å. 1982, A&A, 107, 1
———. 1985, in Theoretical Problems in High Resolution Solar Physics, MPA/LPARL Workshop, ed. H. U. Schmidt (Garching: Max-Planck-Inst.), 1
Nordlund, Å., & Stein, R. F. 1990, Comput. Phys. Commun., 59, 119
———. 2000, ApJ, submitted
Ploner, S. R. O., Solanki, S. K., Gadun, A. S., & Hanslmeier, A. 1998, Space Sci. Rev., 85, 261
Rast, M. P. 1995, ApJ, 443, 863
———. 1998, J. Fluid Mech., 369, 125
———. 1999, ApJ, 524, 462
Restaino, S. R., Stebbins, R. T., & Goode, P. R. 1993, ApJ, 408, L57
Rimmele, T. R., Goode, P. R., Harold, E., & Stebbins, R. T. 1995, ApJ, 444, L119
Rutten, R. J., & Uitenbroek, H. 1991, Sol. Phys., 134, 15
Skartlien, R. 2000, ApJ, 536, 465
Stein, R. F. 1967, Sol. Phys., 2, 285
Stein, R. F., & Nordlund, A. 1998, ApJ, 499, 914
———, ApJ, submitted
Steiner, O., Grossmann-Doerth, U., Knoelker, M., & Schuessler, M. 1998, ApJ, 495, 468